MICROSTRUCTURES AND PHYSICAL PROPERTIES OF FAULT GOUGES FROM AMPHOE KHAO KHO, CHANGWAT PHETCHABUN

Miss Sasithorn Chornkrathok

A Report Submitted in Partial Fulfillment of the Requirements
for the Degree of the Bachelor of Science in Geology
Department of Geology
Faculty of Science
Chulalongkorn University
Academic Year 2015

โครงสร้างระดับจุลภาคและคุณสมบัติทางกายภาพของผงรอยเลื่อน

จากอำเภอเขาค้อ จังหวัดเพชรบูรณ์

นางสาวศศิธร ชอนกระโทก

หัวข้องานวิจัย	โครงสร้างระดับจุลภาคและคุณสมบัติทางกายภาพของ
	ผงรอยเลื่อนจากอำเภอเขาค้อ จังหวัดเพชรบูรณ์
ผู้ทำการวิจัย	นางสาวศศิธร ชอนกระโทก
อาจารย์ที่ปรึกษาโครงการ	อาจารย์ ดร. วรัญทร คณิตปัญญาเจริญ
อาจารย์ที่ปรึกษาร่วมในโครงการ	Professor Dr. Hans-Rudolf Wenk
ภาควิชา	ธรณีวิทยา
ปีการศึกษา	2558

        ผงรอยเลื่อนเกิดจากการบดและขัดสีกันของหินทั้งสองฝั่งของรอยเลื่อน มักมีเนื้อละเอียด อุดมไปด้วยแร่ดิน แม้ว่าผงรอยเลื่อนจะมีอยู่เป็นปริมาณมากในประเทศไทยแต่การศึกษาถึงโครงสร้าง ทางจุลภาคของผงรอยเลื่อน โดยเฉพาะอย่างยิ่งการจัดเรียงตัวจำเพาะของแร่ดินในผงรอยเลื่อนซึ่งถือ ว่าเป็นปัจจัยสำคัญต่อพฤติกรรมการเลื่อนของรอยเลื่อนนั้นยังไม่มีอย่างแพร่หลาย ยกตัวอย่างเช่น แร่ ดินเหนียวชนิดสเม็คไตต์ ซึ่งสามารถดูดซับน้ำไว้ในโครงสร้าง ทำให้ผงรอยเลื่อนเกิดการพองตัว เลื่อน ตัวและความสามารถเชื่อมแน่น งานวิจัยชิ้นนี้จึงมีวัตถุประสงค์เพื่อศึกษาโครงสร้างระดับจุลภาคและ การเรียงตัวจำเพาะของแร่ในผงรอยเลื่อนและหินท้องที่ที่อยู่ในบริเวณใกล้เคียงรอยเลื่อนในพื้นที่ อำเภอเขาค้อ จังหวัดเพรชบูรณ์ ริมทางหลวงหมายเลข 12 ตัวอย่างทั้ง 10 ตัวอย่างจะถูกเก็บมาศึกษา แร่องค์ประกอบ ปริมาณ และการเรียงตัวจำเพาะของแร่โดยใช้เครื่องเร่งอนุภาคชนิดซินโครตรอน โดยวัดด้วยเทคนิคการเลี้ยวเบนรังสีเอกซ์ ผลจากการทดลองแสดงให้เห็นว่าผงรอยเลื่อน มีค่าการ จัดเรียงตัวอยู่ในระดับต่ำ (1.19-2.35) ในขณะที่ค่าการจัดเรียงตัวของหินท้องที่มีค่าตั้งแต่ระดับต่ำถึง สูง (1.14-3.87) ผงรอยเลื่อนในการศึกษาครั้งนี้ประกอบไปด้วยแร่ดินเหนียวหลัก ๆ อยู่ 3 ชนิด คือแร่ ดินประเภทเคโอลิไนต์ อิลไลต์-ไมก้า และ อิลไลต์ที่-สเม็คไตต์ ประมาณ 68 เปอร์เซ็นต์ แม้ว่าผงรอย เลื่อนจะมีปริมาณแร่ดินที่สูง แต่ผงรอยเลื่อนกลับมีค่าการจัดเรียงตัวที่ต่ำเมื่อเปรียบเทียบกับหินเหย้า โดยอาจจะเกิดจากการเลื่อนตัวของชั้นหิน ทำให้การเรียงตัวของแร่เดิมในหินถูกทำลาย ยิ่งไปกว่านั้น ยังพบวัตถุอสัณฐาน ในผงรอยเลื่อน ซึ่งอาจเป็นผลมาจากการบดขยี้ตัวของหิน อีกด้วย นอกจากนี้ใน การศึกษาโครงสร้างระดับจุลภาคโดยใช้กล้องจุลทรรศน์อิเล็กตรอนความละเอียดสูงแบบส่องกราด แสดงให้เห็นถึงร่องรอยการแตกของเม็ดแร่ควอตซ์ และการสะสมตัวของแร่เกอไทท์ ซึ่งบ่งบอกถึง กระบวนการเปลี่ยนรูปและการแปรเปลี่ยนสภาพของหินโดยน้ำแร่ร้อนในผงรอยเลื่อน สิ่งซึ่งบอกถึง การเพิ่มขึ้นของอุณหมูมิและความดันและการเคลื่อนที่ของแนวซึ่งเกิดจากการเกิดรอยเลื่อน และทำให้ หินในบริเวณใกล้เคียงได้รับผลกระทบจากการเลื่อนตัวด้วยเช่นกัน

คำสำคัญ: โครงสร้างระดับจุลภาค การเรียงตัวจำเพาะ แร่ดินเหนียว ผงรอยเลื่อน

Project title (English)	MICROSTRUCTURES AND PHYSICAL PROPERTIES OF FAULT GOUGES FROM AMPHOE KHAO KHO, CHANGWAT PHETCHABUN
Project title (Thai)	โครงสร้างระดับจุลภาคและคุณสมบัติทางกายภาพของผงรอยเลื่อน จากอำเภอเขาค้อ จังหวัดเพชรบูรณ์
Student:	Sasithorn Chornkrathok
Advisor:	Dr. Waruntorn Kanitpanyacharoen
Co-Advisor:	Professor Dr. Hans-Rudolf Wenk

Fault gouge is formed due to tectonic forces along the fault and mainly composed of clay mineral. Despite an abundance of fault gouges in Thailand, relatively little is known about their microstructures and crystallographic preferred orientation (CPO) or fabrics of clay minerals, which play an important role in fault behavior. For example, smectite has an ability to absorb water to its structure, causing fault gouge to swell, slip, and reduce the cohesiveness of the fault gouge. This study is thus aimed to study microstructures and CPO of fault gouges and their host rocks from the fault on Highway-12 in Khao Kho area, Phetchabun. A total of 10 samples were collected to investigate mineral composition, volume fractions, and CPO by synchrotron X-ray diffraction. Results show that the CPO of fault gouges are weak and asymmetric with maxima for (001) ranging from 1.19 to 2.36 multiples of random distribution (m.r.d.). while the CPO of host rocks are from weak to quite high ranging from 1.14 to 3.87 m.r.d. Dominant clay minerals include kaolinite, Illite-mica, and Illite-smectite (68%). Despite having high clay content, fault gouges have lower magnitudes of CPO than host rocks possibly due to fault movements that largely disrupt initial CPO. In addition, an amorphous phase is observed in fault gouges, which may have resulted from the comminution of clasts (crush-origin pseudotachylytes). To further describe the microstructures, selected areas on the samples were further analyzed with Scanning Electron Microscopy (SEM). The presence of deformed quartz grains and goethite veins indicates deformation and hydrothermal alteration process in the fault gouges, implying aggressive fault movement. The host rocks are moderately deformed due the tectonic forces.

Key words: microstructure, crystallographic preferred orientation, clay mineral, fault gouge

ACKNOWLEDGEMENTS

CONTENTS

LIST OF FIGURE

LIST OF FIGURE (CONT.)

LIST OF TABLE

Chapter 1: Introduction

Fault gouge generally refers very fine-grained material produced by cataclasis during tectonic movement. Clay minerals are the dominant mineral group in the fault gouge. Alignment pattern of clay minerals is mainly in 001 plane as perfect cleavage, which shows that clay minerals in many rocks have preferred orientation due to compaction process of sedimentary rock or reprecipitation process under stress. Several studies have focused on the characterization of preferred orientation of clay minerals in fault gouges in various fault zones; for examples, the San Andreas Fault in USA, and the Bogd fault in Mongolia. Preferred orientation of fault gouges from these areas is very week due to aggressive fault movements (Wenk *et al*., 2010; Janssen *et al*., 2012; Buatier *et al*., 2012 respectively). However, the investigation of clay minerals on shear strength is still controversial because clay minerals are extremely small grain size as well as there are mixed layers of different clay minerals, which is difficult to study precipitation and orientation of clay mineral. Thus, these controversy raises doubt about the microstructure and physical properties of the fault, which contribute to this research. If microstructure and physical property, especially preferred orientation of mineral in fault gouge were made clear, this data can be applied to other research such as fault movement or fault trap in this area effectively and efficiently.

This project is thus aimed to study microstructure, mineralogy, and crystallographic preferred orientation (CPO) of minerals in fault gouges and host rocks in fault zone from Khoa Kho area, Phetchabun province, Thailand.

A number of previous studies investigate the CPO of clay-rich rocks and fault gouges. For example, a study by Wenk *et al*. (2010) compares the preferred orientation of phyllosilicates between the San Andreas Fault (SAF) gouge, shale and schist by using Scanning Electron Microscopy (SEM) and Synchrotron X-ray diffraction (Syn-XRD) in order to investigate alignment pattern and overlapping diffraction peaks of mineral in all samples in high resolution. The results suggest that fault gouges have lower magnitudes of CPO than those of deeply-buried shale and schists. The presence of minerals in the SAF gouge such as analcite, talc, serpentine and amorphous silica also indicates alteration and reprecipitation at low-grade metamorphism by hydrothermal fluids. There is the strongest preferred orientation of minerals in schists. It may result from deformation and recrystallization in metamorphic rock. There is also preferred orientation in shale samples due to shale has fissility which comes from precipitation of phyllosilicate. To sum up, Advance in X-ray diffraction technique can investigate not only overlapping diffraction peaks in (001) plane of minerals in all samples but also in all case.

The physical properties of clay fabrics in San Andreas Fault observatory at depth core samples was mentioned by Janssen *et al*. (2012). The microstructure of samples was analyzed by using SEM and Transmission Electron Microscopy (TEM). The CPO of mineral was investigated by using Syn-XRD in order to understand

orientation pattern of clay gouge. SEM and TEM images illustrate two patterns of clay minerals: microstructure such as fold and kinking, and newly form of mineral. Kinking and fold of phyllosilicate minerals produced by faulting spread in the matrix and randomly wrap rounded other grains during shear deformation as clay-clasts aggregates (CCAS) (Boutareaud et al., 2010). The newly formed clay minerals grew in various orientations in the pore between each mineral grain suggesting reprecipitation of mineral during hydrothermal alteration. Compared with texture of phyllosilicate mineral in shale and mudstone (2-10 m.r.d.) which are host rocks in this area, texture of clay minerals is very weak and asymmetric, suggesting faulting process. Friction coefficient was reduced by sheet silicate which was found along slip zone (e.g. Solum et al., 2010). In addition, changing of gouge fabrics in fault slip zone may change the mechanical properties and strength of the fault. (Vrolijk and van der Pluijm, 1999).

The study by Buatier et al. (2012) uses x-ray powder diffraction (XRD), SEM and TEM, and Syn-XRD to investigate microstructure and preferred orientation from Bogd fault gouge, Mongolia in order to study the origin and behavior of clay minerals in Bogd fault gouge. SEM images illustrate microstructure of samples which was divided two groups: cataclastic zone and fault gouge zone. The cataclastic zone shows the occurrence of authigenic kaolinite which mostly randomly oriented that fills between pore or fragmented quartz grain. Homogeneous microstructure of clay gouges illustrates two main types: foliated and isotropic gouge. Foliated show orientation of clay mineral and isotropic microstructure show an alternating texture. Compared with smectite and illite-mica, texture of kaolinite has a stronger than other minerals in all sample. Kaolinite comes from precipitation or recrystallization from aluminum-rich minerals while illite-mica come from weathering and erosion of muscovite. Smectite can interact with water which contributes to dehydration. That behavior is the cause of transition of smectite-to-illite (illitization of smectite), which make CPO change. The result of dehydration contributes to change the frictional resistance (Morrow et al., 2000). The result suggests that the CPO of clay mineral which is the major component of the gouge (Vrolijk & van der Pluijm, 1999) can play an important role in fault behavior.

To better establish a comprehensive understanding of the physical properties of clay-rich rocks, this study thus aims to compare CPO and clay content of fault gouges and host rocks. The methodology is divided into two parts. The first, microstructures and mineral compositions are evaluated by using SEM. The second method is Syn-XRD for measuring the degree of mineral preferred orientation and their volume fractions. If we understand the pattern of microstructure and crystallographic preferred orientation of minerals in fault gouge and host rocks, we can explain the relationship between the crystallographic preferred orientation of minerals in fault gouges and the host rocks.

Chapter 2: Study area and Methodology

2.1 Study area

2.2 Physical geography and geology of Phetchabun

    2.2.1 Geographic feature

    2.2.2 Geology

        2.2.2.1 Stratigraphy of Phetchabun province

2.3 Geological setting and sample collections

2.4 Experimental methods

    2.4.1 Scanning Electron Microscope (SEM)

    2.4.2 Synchrotron X-ray diffraction

2.1 Study area

The study is an outcrop on Highway 12 in Khaem Son sub-district, Khao Kho district, Phetchabun province. Geographic coordinate system is 16°46'50.93" N and 100°59'50.64" E (Figure 2.1).
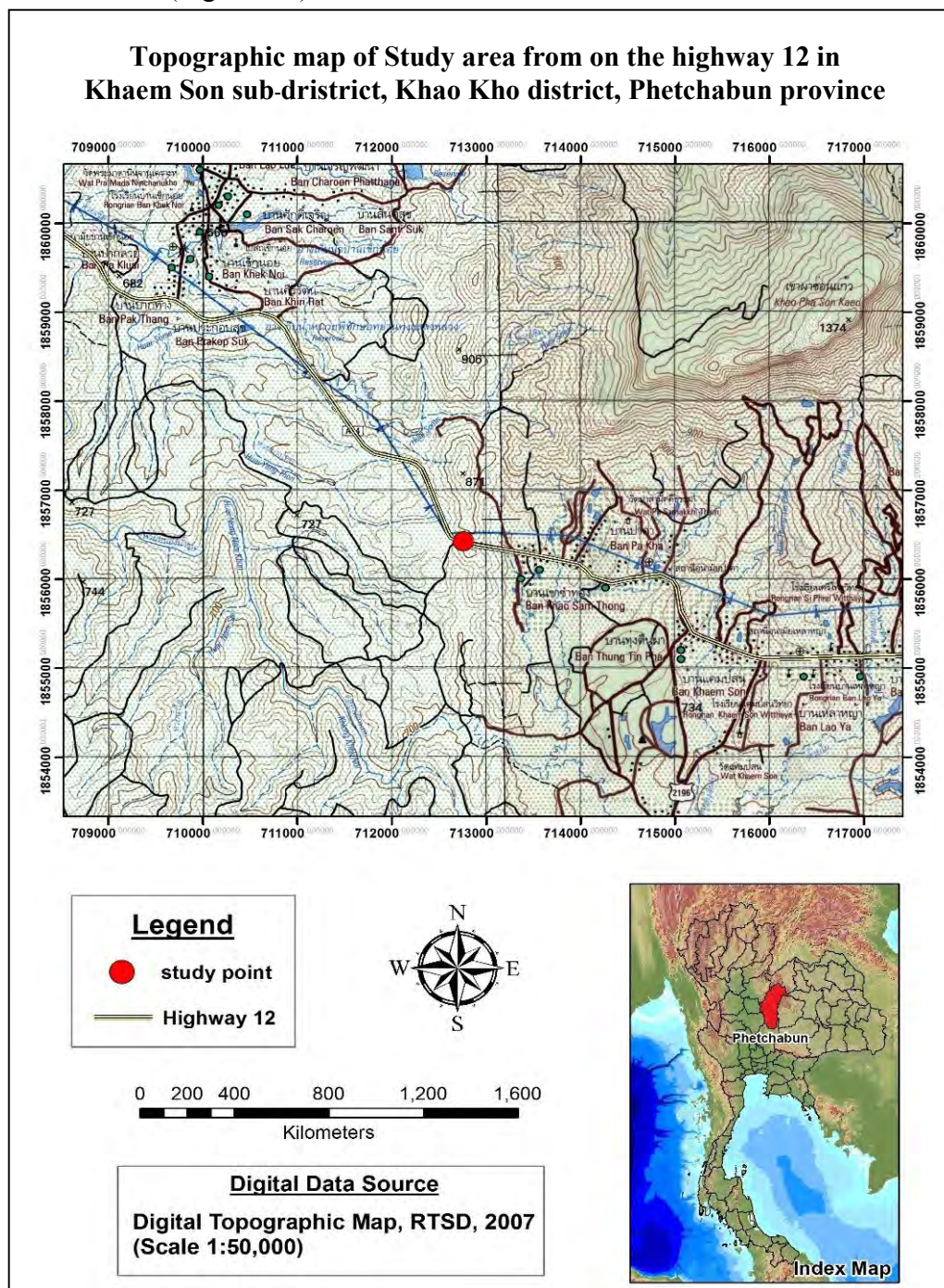
Figure 2.1 Topographic map illustrates the location of study point which is located on highway 12 in Khaem Son sub-district, Khao Kho district, Phetchabun province (Royal Thai Survey Department, 2007).

2.2 Physical geography and geology of Phetchabun

      2.2.1 Geographic feature

Phetchabun province is located in the Northern part of Thailand, which is a boundary between the North, Northeast, and Center of Thailand. It is situated between latitude and longitude of 16°N and 101°E. There are 12,668.42 square kilometers in Phetchabun area. The widest part measured from east to west is 55 kilometers long and the longest part from north to south is 296 kilometers. The topography of Phetchabun province consists of Phetchabun mountain range which resembles a horseshoe shape. The mountain surrounds the north of the province, which is parallel to both the east and west (Figure 2.2) (DMR, 2009).

      2.2.2 Geology

         2.2.2.1 Stratigraphy of Phetchabun province

Phetchabun province is located on the northwestern margin of the Khorat Plateau and one part of Loei-Phetchabun fold belt, which contributes to different rock types of Phetchabun and surrounds rock age from Carboniferous to Quaternary (350 million years old - Recent). The geology of Phetchabun is illustrated by recently geological map sheet Phetchabun, scale 1:250,000 Compiled by kitti khaowiset and Narin Chanfoo, Department of Mineral Resources in 2009. The rock types are composed of sedimentary rock, metamorphic rock, igneous rock, and unconsolidated sediments (Figure 2.2).

      Carboniferous Unit

      This unit consists of Wang Sa Phung Formation. This formation was found on the mountain on the west side of the province. It consists of conglomerate, shale, and sandstone interbedded with limestones and volcanic rocks.

      Permo-Carboniferous Unit

      This unit is composed of sandstone, siltstone, shale, mudstone, conglomerate bed and slaty shale. It was found on the west side of the province.

      Permian Unit

      This unit is composed of 4 formations: Tak Fa Formation (P_{tf}), Pha Nok Khao Formation (P_{pn}), Hua Na Kham Formation (P_{hn}), and Nam Duk Formation (P_{nd}), which is in Saraburi Groups. P_{tf} consists of massive gray to black limestone, black nodular or thin bedded chert. P_{pn} is composed mainly of massive gray limestone and dolomite, and thin-bedded gray shale. P_{hn} is made up of intercalated light and dark gray siltstone, sandstone, claystone, and limestone. P_{nd} consists mainly of pelagic shale, clastic turbidites, and thin-bedded allodapic limestone.

Triassic Unit

This unit consists of 7 formations of Khorat group: Huai Hin Lat Formation (Tr_{hl}), Nam Phong Formation (Tr_{np}), Phu Kradung Formation (J_{pk}), Phra Wihan Formation (JK_{pw}), Sao Khua Formation (K_{sk}), Phu Phan Formation (K_{pp}), and Khok Kruat Formation (K_{kk}). Tr_{hl} is composed of sandstone, siltstone, shale, sandstone and limestone, and conglomeratic sandstone. Tr_{np} consists of resistant, reddish brown, micaceous sandstones, conglomerates, siltstone and mudstone of mainly fluvial origin. J_{pk} is made up of soft, micaceous, reddish-brown and grayish-red siltstone with greenish-gray calcareous conglomerate beds. Interbedded with greenish gray feldspathic medium-grained sandstone. JK_{pw} consists mainly of white, yellowish, light brown sandstones, less abundant grayish-red siltstone and rare green or dark red clay. K_{sk} is composed of an alternation of grayish-reddish brown siltstone and clay and fine to medium-grained pale red to yellowish-gray sandstone. Rare pale red to light gray conglomerates, containing carbonate pebbles, are also characteristic of this Formation. K_{pp} consists of fine to coarse-grained and conglomeratic sandstone containing rounded pebbles of quartz and chert. K_{kk} is made up of red siltstone interbedded grayish-red sandstone and calcareous conglomerate with limestone clasts.

Quaternary Unit

Quaternary are represented by alluvial deposit (Qa), terrace deposit (Qt), and colluvial deposits. Qa was found in the central plains of the province. Qt was found along the river in the central plains of the province. Qc was found at the base of mountains in the western part of the province.

Igneous rock Unit

Igneous rock in this province was divided into 4 groups: volcanic rock in Permian period, volcanic rock in Permo-Triassic period, plutonic rock in Triassic period, and volcanic rock in Tertiary period. Volcanic rock in Permian period consists of grayish green andesite porphyry and pale gray rhyolite porphyry. Volcanic rock in Permo-Triassic period is composed of rhyolite tuff, tuff, andesitic tuff. It was found in the north, center and west side of the province. Plutonic rock in Triassic period consists of verities of granite. It was found on the west side of the province. Volcanic rock in Tertiary period consists of dark gray to black basalt, grayish red rhyolite, and fine grain grayish green andesite. It was found on the south side of the province

Based on DMR (2009), it is concluded that the study area is in Phu Kradung Formation of the Khorat Group. The sample is in Jurassic. Reddish-brown and grayish-red siltstone with greenish-gray calcareous conglomerate beds interbedded with greenish-gray feldspathic medium-grained sandstone are commonly found throughout the Phu Kradung Formation (DMR, 2009) (Figure 2.3)

Figure 2.2 Geological map of Phetchabun (DMR, 2009)
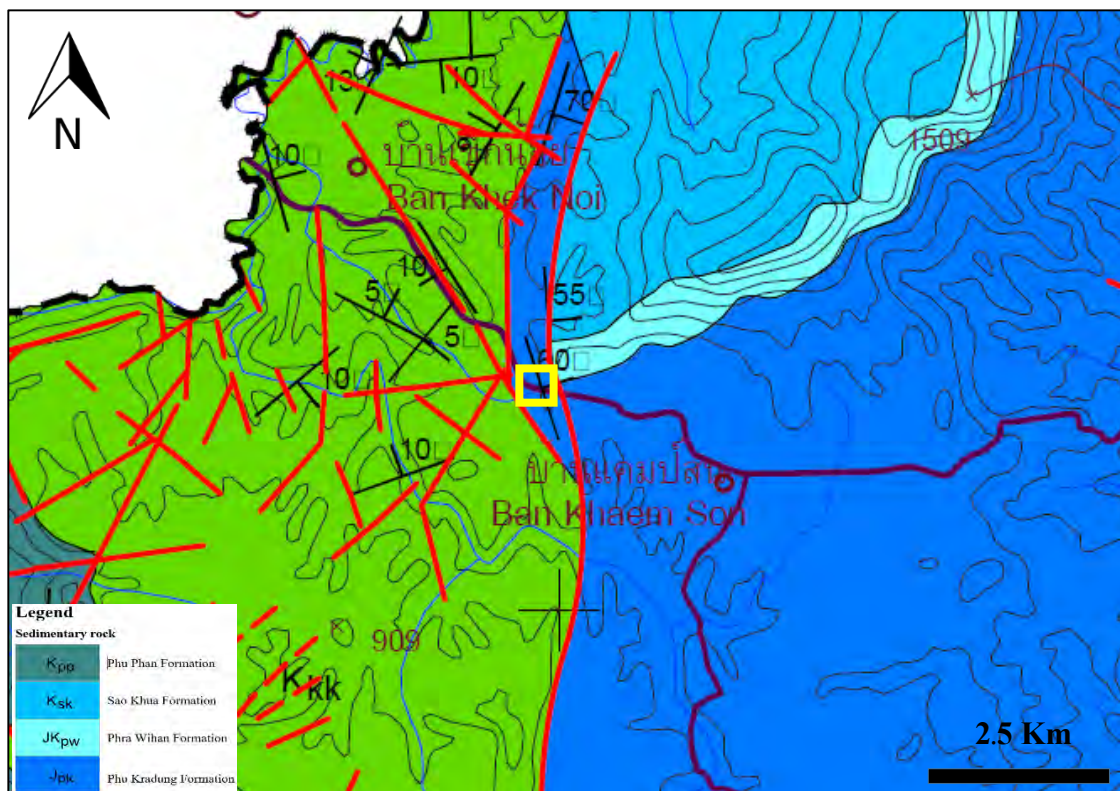
Figure 2.3 Geology of the study area (inside the yellow line) illustrated by (Modified from DMR, 2009)

2.3 Geological setting and sample collections

A total of samples were collected from two main zones in the study area. four samples were chosen from the fault gouge zone and six samples were collected from the host rock (Figure 2.4). The samples are in Jurassic Phu Kradung Formation of the Khorat Group, which is the main sedimentary process in the continental plate (DMR, 2009). There is an almost vertical fault in the sampling area illustrated as a yellow line in Figure 2.4. It might have been affected by the occurrence of Loei-Petchabun Fold Belt which was re-activated during the end of the Permian and Early Triassic (Sattayarak, 1985; Cooper *et al.*, 1989)
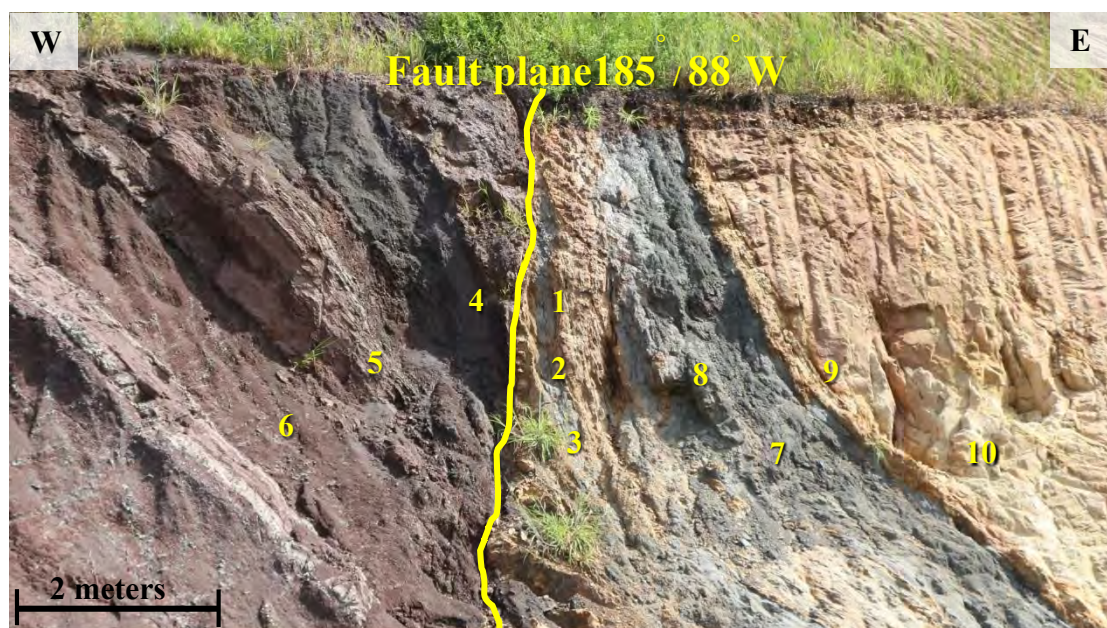
Figure 2.4 Outcrop of this study on highway 12 in Khaem Son sub-district, Khao Kho district, Phetchabun province. A geographic coordinate system is $16°46'50.93''$ N and $100°59'50.64''$ E. The fault plane and sampling location are labeled as a yellow line and number, respectively.

2.4 Experimental methods

The experimental procedures were divided into two parts: Scanning Electron Microscopy and Synchrotron X-ray diffraction

2.4.1 Scanning Electron Microscope (SEM)

This experiment is planned to examine the microstructures of different components in fault gouges and the host rocks in the fault zone. Though these samples both include a large volume of clays, the internal structure and compaction information are expected to be different and can be observed in Scanning Electron Microscopy (SEM) images.

The samples were embedded in epoxy resin in a plastic box overnight to produce epoxy cylinder approximately 2 cm in diameter (Figure 2.5). After that, they were made into thin sections. The polished thin sections of all samples were coated with carbon (Figure 2.6) in order to improve the imaging quality. Carbon helps create a conductive layer of metal on the sample in the SEM experiment, which inhibits charging.

All samples were examined with ZEISS EVO MA10 high vacuum SEM system, which is equipped with an EDAX Energy-Dispersive Spectroscopy (EDS) (Figure 2.7) (Kanitpanyacharoen *et al.*, 2011). The samples were evaluated for surface topography and the elemental composition. The backscattered electron (BE) SEM image illustrates complex microstructure of the samples based on atomic number material. Material with high atomic number material appears brighter than low atomic number material in a backscattered electron image. The EDAX Genesis Maps/ line was used to collect

chemical composition of the samples such as Si, O, Mg, Al, Fe, K, C and other elements.
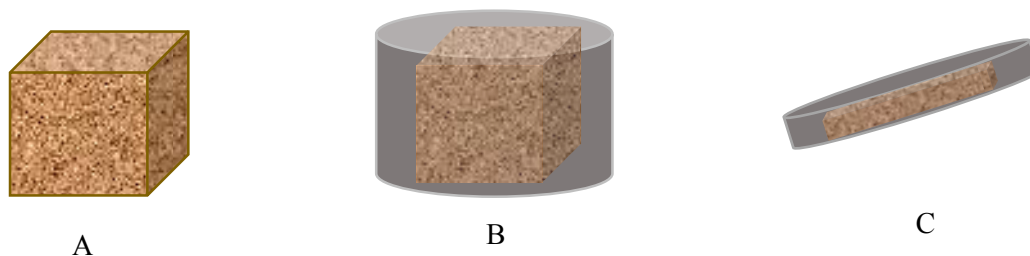
Figure 2.5 (A) Preparing the samples in order to have a diameter and height (or thickness) at most 2 cm. (B)Casting the samples into a cylindrical shape. (C) Polishing the sample to make them thinner than 2 mm

Figure 2.6 Carbon coating equipment (A) Carbon coating equipment, (B) The inside of Carbon coating equipment and (C) Polished thin section, coated with carbon

**Figure 2.7** ZEISS EVO MA10 Scanning Electron Microscope (SEM) equipment

2.4.2 Synchrotron X-ray diffraction

The samples were embedded in epoxy resin in a plastic box overnight to produce epoxy cylinder approximately 2 cm in diameter (Figure 2.5). They were polished into thinner than 2 mm in order to use in X-ray diffraction experiment. This method is used to measure the degree of mineral preferred orientation and their volume fractions in the samples.

The samples were analyzed on the high-energy beamline BESSRC 11-ID-C of the Advanced Photon Source (APS) at Argonne National Laboratory (Chicago, Illinois, USA) (Wenk *et al*., 2007), with a monochromatic wavelength of 0.10798°A. The diffraction images were recorded for 60 seconds with the Mar 345 image plate detector (3450 x 3450) about 2 m away from the samples, in the pattern of Debye rings, at eleven different ω tilt angles (Figure 2.8). The samples were rotated around the horizontal axis in 15° increments (-75°, -60°, -45°, -30°, -15°,0°, 15°, 30°, 45°, 60°, 75°). The intensity variations along the Debye rings illustrates the presence of preferred orientation of mineral of the samples (Figure 2.9) (Wenk *et al*., 2007). The diffraction images were calibrated distance from sample to detector and orientation by Lanthanumboride standard for instrument file. The diffraction images shown in Q-spacing ($Q = 2\pi/d$) in order to clearly distinguish the peak positions were integrated from 0° to 360° azimuths over 10° intervals to produce 36 spectra (Kanitpanyacharoen *et al*., 2012). Q-spacing ranged from 0.4 to 5 Å. Each spectrum represents differently oriented lattice planes. X-ray diffraction data will be quantified with the Rietveld

Analysis (Rietveld, 1969) implemented in MAUD (Material Analysis Using Diffraction) software (Lutterotti *et al*., 1997) This is the process of data analysis after the image was already transformed from .tiff file to. esg file in MAUD program as follows:

1. Refine Background polynomial parameter (three times for each spectrum).
2. Add instrument file (.inf file)
3. Import phase of mineral (in this case is Quartz)
4. Choose Fix all parameter, free background, and free scale parameter command from parameter list
5. Choose launch parameter refinement (refine)
6. Click datafileset_x (diffraction image) in order to add term of background peak (depend on each sample) in background function
7. Refine Hight, HWHM, and HWHM(eta) for all background peak
8. Import other phases based on peak position of the phase and refine one by one (don't forget to free scale parameter). The datafiles can be found in the American Mineralogist Crystal Structure database and MAUD database
9. Change unique axis from "B" of monoclinic phase (e.g. Illite or dickite) to "C" and refine all cell parameter of that mineral
10. Refine crystallite size and R. m. s. microstrain in Size-Strain model option from microstructure of each mineral
11. Choose free microstructure from parameter list
12. Examine the accuracy of microstructural information and volume fractions for each phase (quantitative phase analysis)
13. Modify EWIMV algorithm which is related to WIMV (Matthies and Vinel, 1982) in order to texture analysis.
14. Combine all eleven computational results of the same sample into one.
15. Calculate texture of phases with preferred orientation by using E-WIMV function with 10° orientation distribution function (ODF) resolution and without generating symmetry.
16. Export the ODF files (.maa), prepare binary (YOM) file, smoothing and sharping the data, calculate display pole Figure using Beartex program.
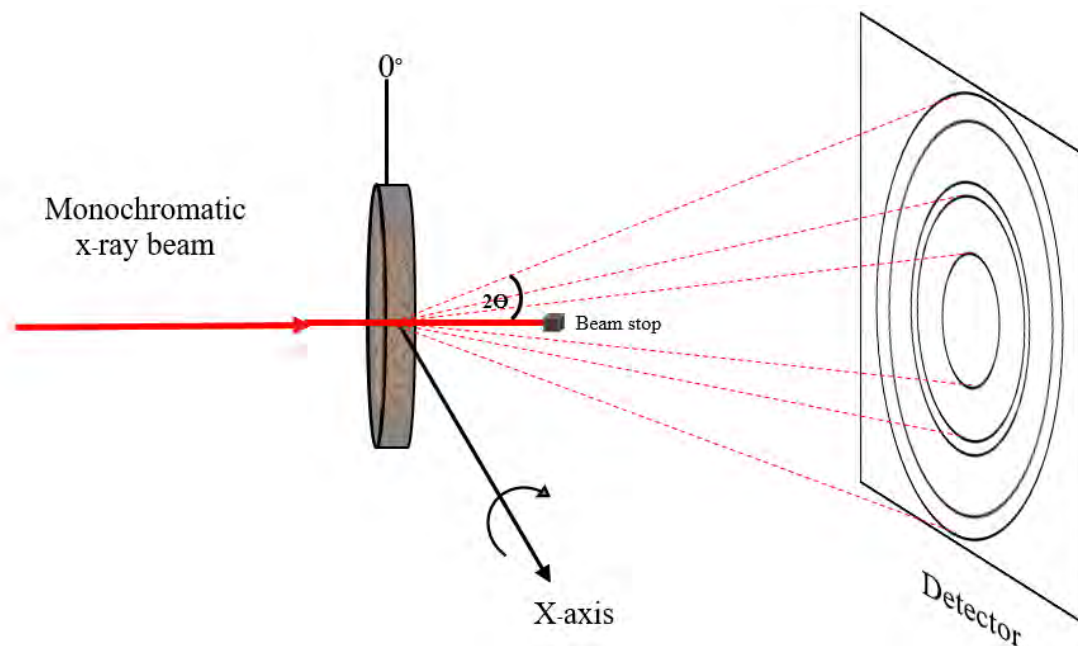
Figure2_8 X-ray experiment on the high-energy beamline BESSRC 11-ID-C of the Advanced Photon Source (APS) (Modified from Kanitpanyacharoen *et al*., 2012)
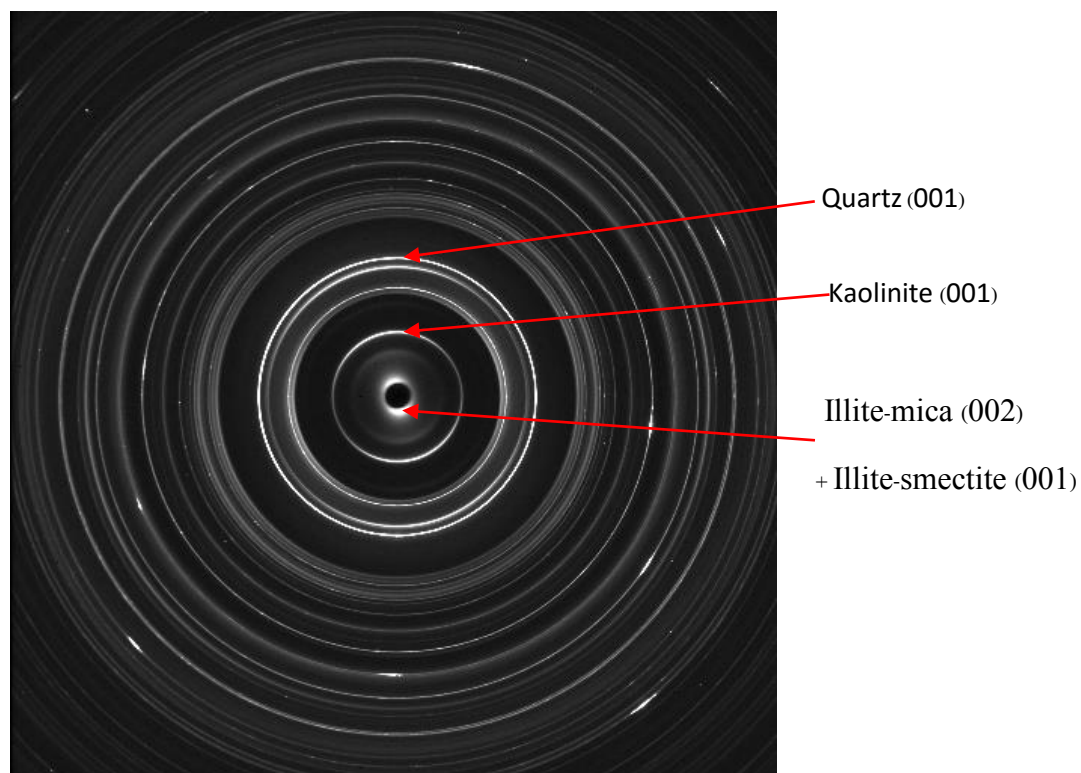
Figure 2.9 Diffraction image illustrates intensity variations along Debye ring, which indicate preferred orientation of mineral. Arrows point to 7.17 A° diffraction of Kaolinite (001), 10 A° diffractions of Illite-mica (002) and Illite-smectite (001), and 3.34 A° diffraction of Quartz (001)

Chapter 3: Results

3.1 Classification of all samples

3.2 Mineralogy and Microstructures

    3.2.1 Fault Zone

        3.2.1.1 Fault gouges

        3.2.1.2 Cataclasite

    3.2.2 Host rocks

        3.2.2.1 Siltstone

        3.2.2.2 Shale

        3.2.2.3 Sandstone

3.1 Classification of all samples

Ten samples are divided into two main groups: fault zone samples and host rock samples. The fault zone samples can be further classified into two groups based on SEM data: fault gouges (sample 1-3) and cataclasite (sample 4) (Rock classification based on Davis and Reynolds, 1996) (Figure 3.1). In addition, host rock samples are sub-divided into three groups: siltstone (sample 5,6), shale (sample 7) and sandstone (sample 8-10) (Figure 3.2).
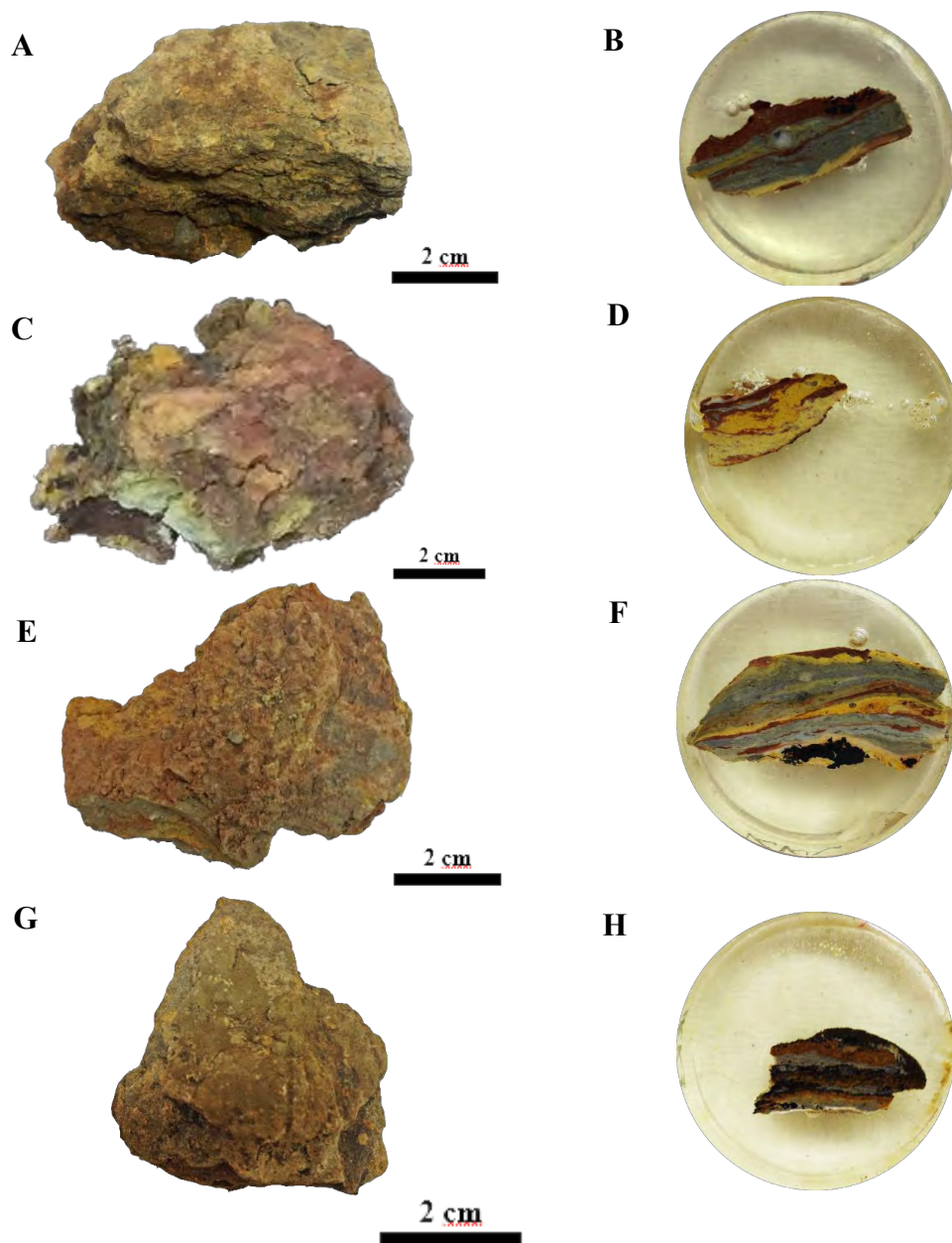
Figure 3.1 Rock samples from fault zone: sample 1 (A, B), sample 2 (C, D), sample 3 (E, F), and sample 4 (G, H).
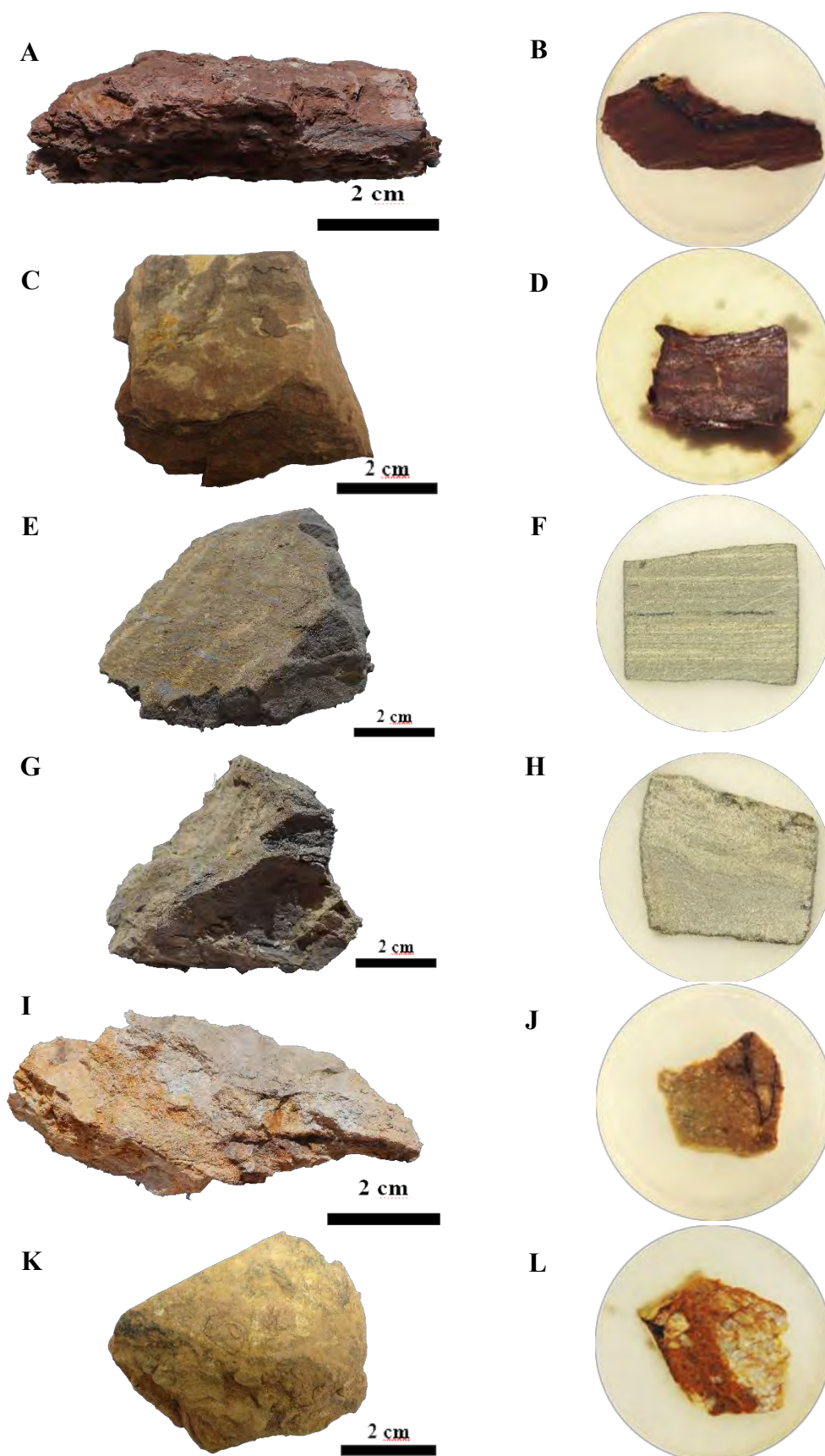
Figure 3.2 Rock samples from host rocks: sample 5 (A, B), sample 6 (C, D), sample 7 (E, F), sample 8 (G, H), sample 9 (I, J), and sample 10 (K, L).

3.2 Mineralogy and Microstructure

Mineral proportion calculated by the Rietveld refinement method are summarized in Table 3.1. Fault samples are dominated by clay minerals (~68%), including kaolinite, illite-mica and illite-smectite. In contrast, host rocks contain mainly of quartz (36-87%). Moreover, most samples are altered by hydrothermal process as indicated by the occurrence of goethite (~9%). In addition, several minor minerals such as anatase, rutile and laumonite are also observed.

In general, phyllosilicates show strong preferred orientation of (001) lattice plane as summarized in Table 3.2 while other minerals show random orientation. The pole densities are measured in multiples of random distribution (m.r.d.). Clay minerals in the shale sample display the highest pole density (2.54-3.87 m.r.d.). In other samples, clay minerals show lower degree of preferred orientation (1.04-2.56 m.r.d.).

Table 3.1 Phase proportion (in weight %) for samples analyzed in this study by MAUD program

	KK1	KK2	KK3	KK4	KK5	KK6	KK7	KK8	KK9	KK10
Kaolinite	36.867	39.053	31.933	7.184	7.118	13.886		10.404	6.185	3.621
Dickite				19.864	7.678		9.043		2.412	4.163
Illite-mica	14.417	16.221	27.442	3.009	15.616	13.52	26.689	23.121	7.156	0.606
Illite-smectite	9.889	8.541	18.591	4.539	7.253	11.209	18.598	3.854	1.442	
Chlorite					5.236	4.254	3.369	3.876		
Quartz	28.818	25.529	16.547	48.451	36.814	53.152	42.301	58.744	65.211	87.454
Hematite	0.654	0.168	0.198	0.236	6.158	3.979			0.872	0.249
Goethite	5.194	6.939	1.107	12.311	14.126				16.725	3.906
Anatase	3.804	3.028	3.631	1.019						
Rutile	0.357	0.52	0.551	0.215						
Laumonite				3.17						

Table 3.2 Pole figure maxima (top) and minima (bottom) (in m.r.d.).

	KK1	KK2	KK3	KK4	KK5	KK6	KK7	KK8	KK9	KK10
Kaolinite	2.36	2.05	2.20	2.61	2.39	1.78		1.32	1.18	1.14
	0.35	0.49	0.40	0.34	0.27	0.51		0.77	0.84	0.08
Dickite				2.17	2.02		2.65		1.19	1.15
				0.53	0.49		0.56		0.08	0.87
Illite-mica	2.08	1.45	2.09	1.37	2.52	2.35	3.87	1.69	1.23	1.04
	0.57	0.75	0.42	0.54	0.30	0.58	0.38	0.58	0.86	0.95
Illite-smectite	1.41	1.19	1.51	1.74	2.53	2.15	2.54	1.47	1.28	
	0.71	0.81	0.39	0.50	0.23	0.68	0.46	0.42	0.84	
Chlorite					2.56	1.66	3.03	1.41		
					0.28	0.83	0.37	0.67		

3.2.1 Fault zone
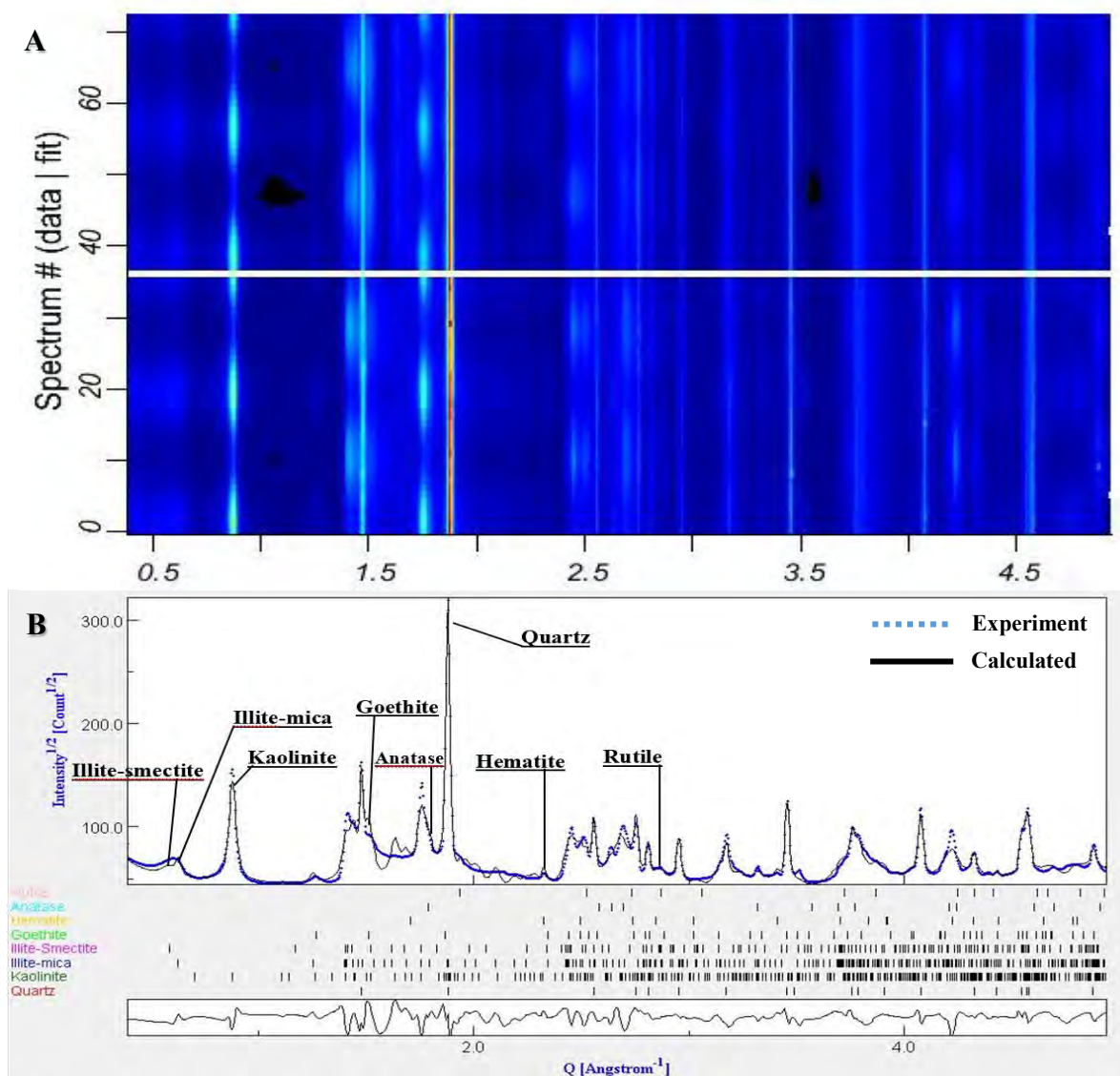
3.2.1.1 Fault gouges

The microstructure of fault gouges is almost homogeneous (Figure 3.3A) due to the abundant fine-grained materials and less amount of quartz (Figure 3.3B). Quartz is highly fractured and has angular shape, suggesting fraction process (Figure 3.3C), while illite illustrates the foliated gouges along the shear zone which indicates shear history (Figure 3.3D). In addition, random distribution of kaolinite (Figure 3.3E) is recognized from high magnification SEM images of the samples. Hollandite is also presented (Figure 3.3F) which suggest that it is a secondary weathering product of earlier manganese-bearing minerals (Biagioni *et al.*, 2012). There is also titanium dioxide (TiO$_2$) in the samples which the TiO$_2$ type can predict temperature and pressure of metamorphism in that area.

Fault gouges are composed of 8 mineral phases (Figure 3.4) from Rietveld analysis, resulted in weight percentages (wt%). All fault gouges samples in this study are composed of similar mineral composition, dominate with kaolinite (32-39 wt%), illite-mica (15-28 wt%), illite-smectite (9-19 wt%), quartz (17-29 wt%), hematite (0.2-0.7 wt%), goethite (1-5 wt%), anatase (3-6 wt%), and rutile (0.4-0.6 wt%), summarized in (table 3.1). Crystallographic preferred orientation (CPO) of the minerals in fault gouges is weak. The pole figures in Figure 3.5 also show asymmetries due to weak texture of phyllosilicate minerals. In addition, there are amorphous materials in these fault gouges (Figure 3.6), which suggest that they may result from friction melting or comminution of clasts (crush-origin pseudotachylytes) (Janssen *et al.*,2010).
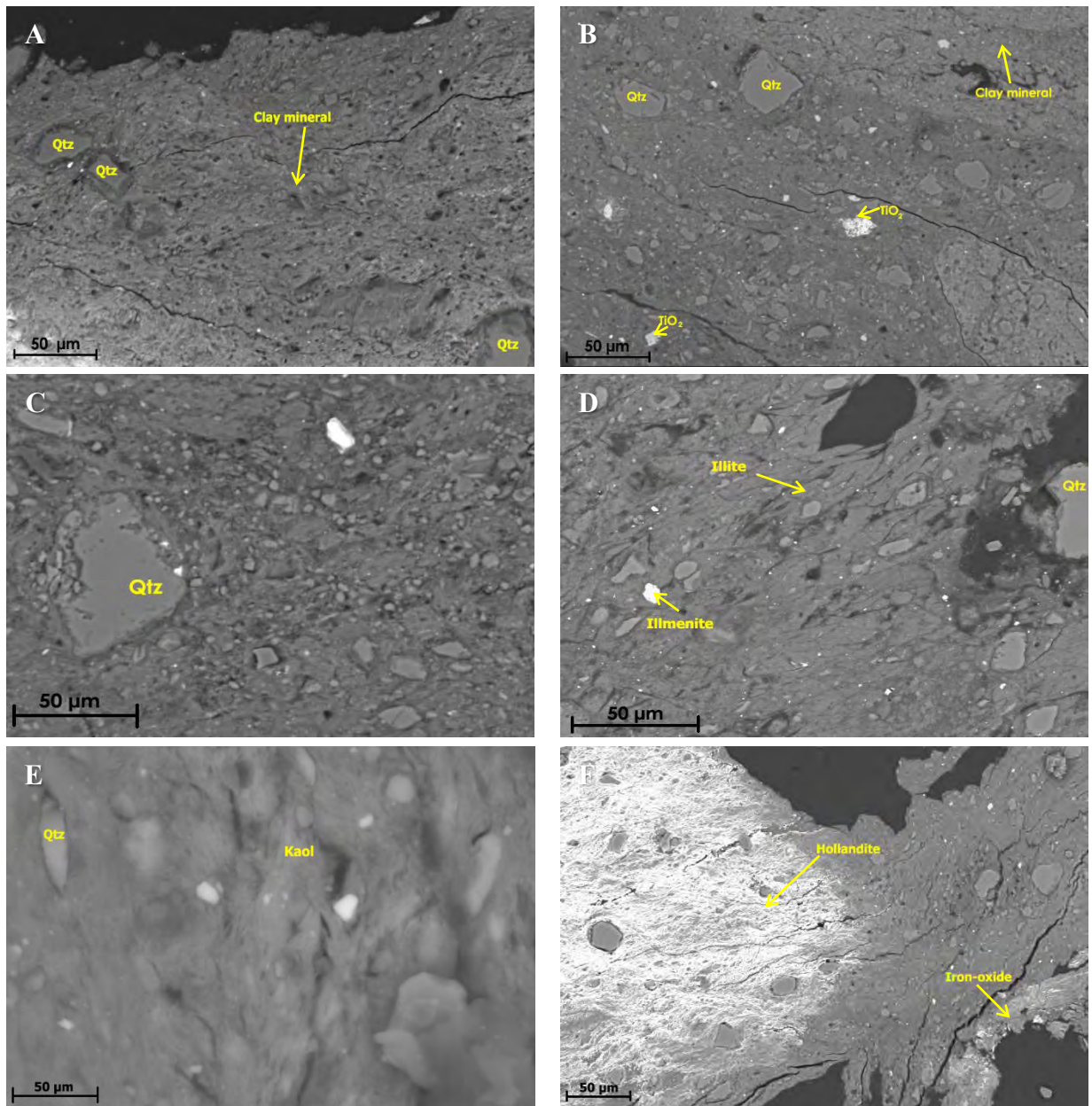
Figure 3.3 SEM-BSE images of fault gouges. (A) Homogeneous microstructure of fault gouges in sample 1. (B) Sample 2 displaying less amount of quartz compared to clay minerals. (C) Fractured quartz grains. (D) Texture arrangement of illite along shear zones. (E) Orientation of kaolinite in high magnification images. (F) Precipitation of hollandite (Mn-bearing mineral). Qtz: quartz, Kaol: kaolinite

Figure 3.4 Diffraction patterns of fault gouges (sample 1). Scale is Q (2π/d). (A) Stack of 36 diffraction spectra in 2D map plots, comparing experimental data (bottom) with calculated spectra (top) for an image taken at 0° tilt and averaged over 10° azimuthal intervals. (B) Average diffraction spectrum. Blue dots are measurements and black solid line is the Rietveld fit. The peak position of contributing phase is indicated at the bottom.
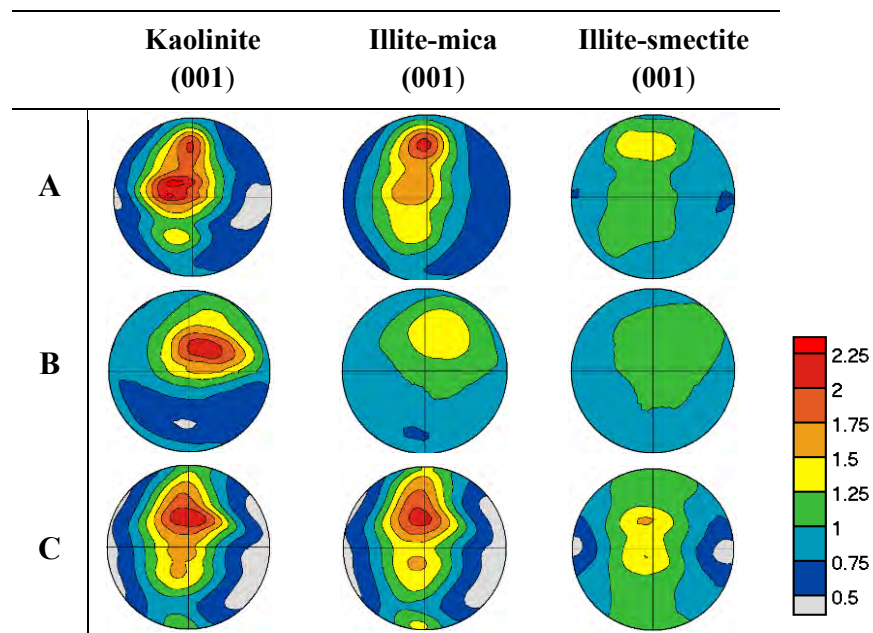
Figure 3.5 (001) pole figures of kaolinite, illite-mica, and illite-smectite of (A) sample 1, (B) sample 2, and (C) sample 3 in the fault gouges. Equal area projections on bedding plane, and contours in multiples of a random distribution (m.r.d).
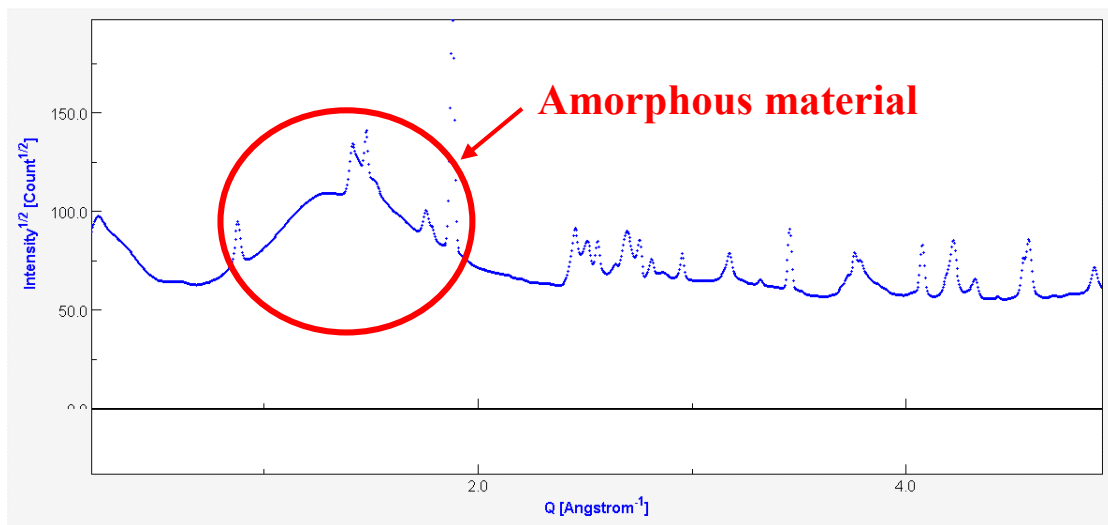
Figure 3.6 Diffraction image of fault gouges illustrates irregular diffraction patterns, suggesting amorphous materials.
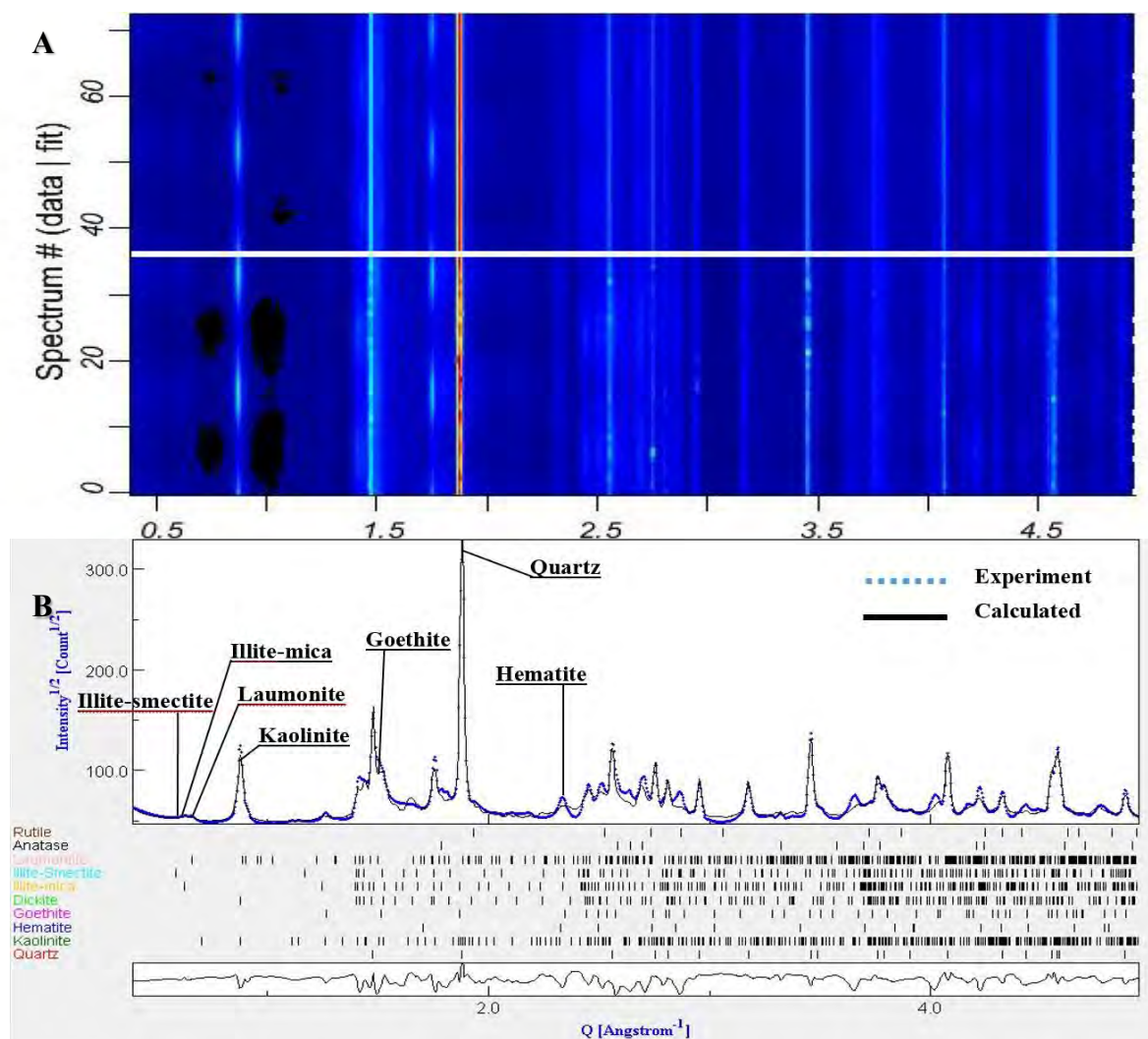
3.2.1.2 Cataclasite

Cataclasite has various grain sizes of quartz which are highly fractured and has angular shape, suggesting fraction process (Figure 3.7A). Clay minerals randomly orientate along the quartz grains. In addition, there is occurrence of authigenic kaolinite group filled in the pores between fragmented quartz grains. Veins of iron oxide crosscut the cataclasite and the iron solution filled the spaces between fragmented quartz grains and fractured zone. This suggest that the veins formed after fault history (Figure 3.7B). Some areas including pores of this sample is filled by hollandite which is presented in bright colors in Figure 3.7C due to its higher electron contract than other minerals in the sample. The presence of hollandite suggest that the mineral is a secondary weathering product of earlier manganese-bearing minerals (Figure 3.7C). In addition, titanium dioxide is also found in this sample its type of TiO_2 can predict the metamorphic temperature and pressure. CPO of fault gouges is weak and shows asymmetry on pole figures with the range of 1.4-2.4 m.r.d. (Figure 3.9). From the Rietveld analysis, mineral composition of sample 3 consists of 10 types (Figure 3.8) explained in (Table 3.1).
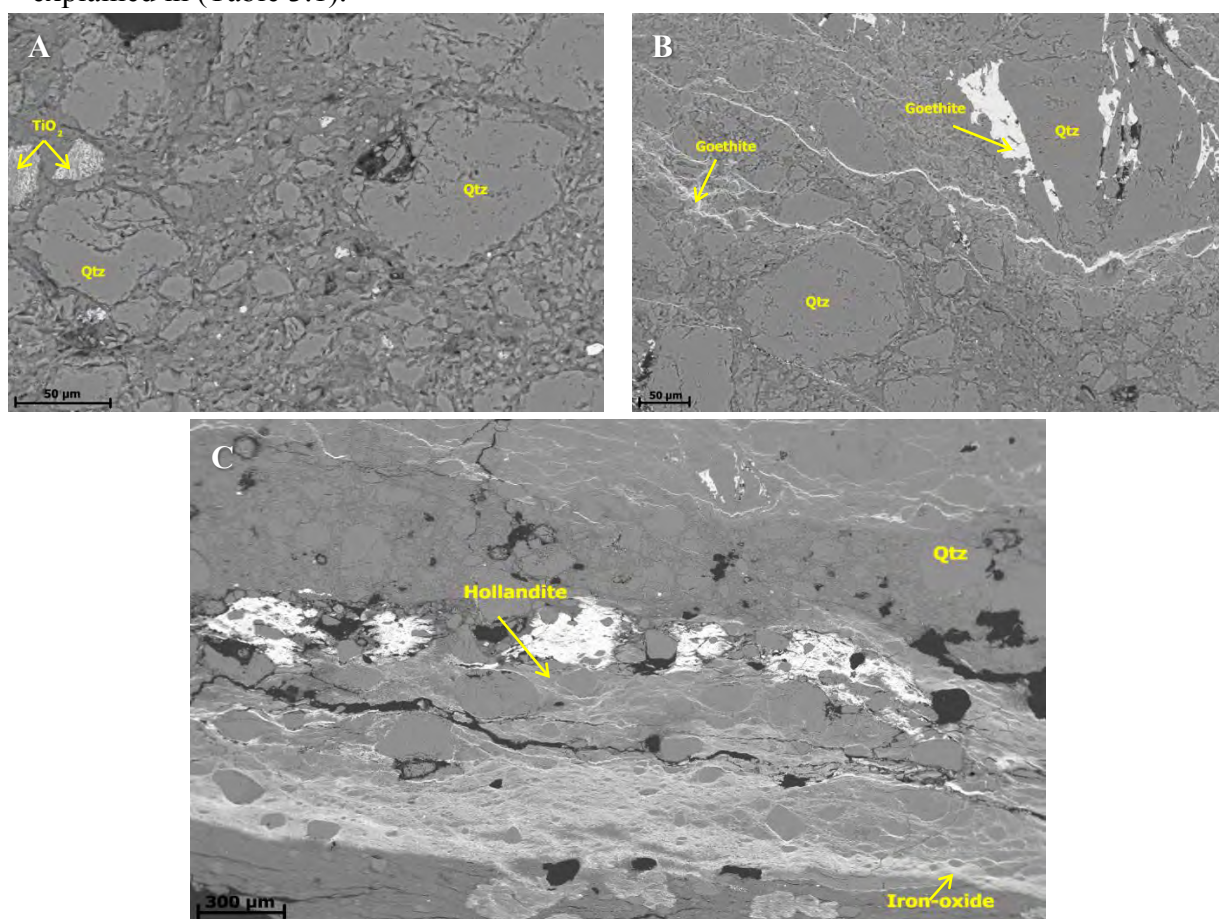

Figure 3.7 SEM-BSE images of cataclasite. (A) Fractured quartz grains. (B) Iron solution fills interstices fragmented quartz grains and fractured zone. (C) Precipitation of hollandite (Mn-bearing mineral) and precipitation of Iron-oxide from Hydrothermal alteration. Qtz: quartz

Figure 3.8 Diffraction pattern of cataclasite (sample 4). Scale is Q (2π/d). (A) Stack of 36 diffraction spectra in 2D map plots, comparing experimental data (bottom) with calculated spectra (top) for an image taken at 0° tilt and averaged over 10° azimuthal intervals. (B) Average diffraction spectrum. Blue dots are measurements and black solid line is the Rietveld fit. The peak position of contributing phase is indicated at the bottom.
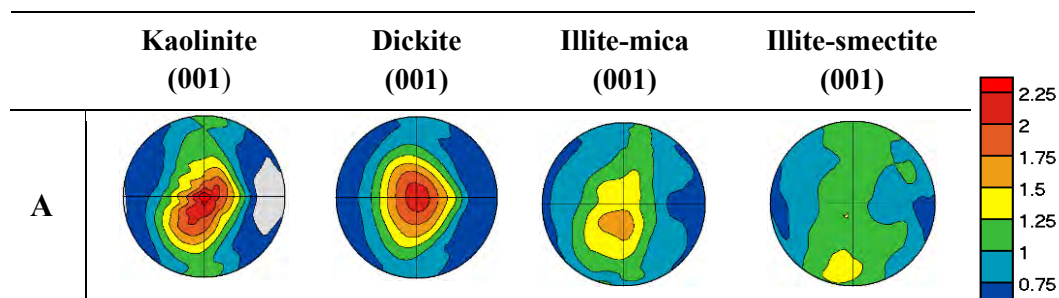

Figure 3.9 (001) pole figures for kaolinite, dickite, illite-mica, and illite-smec cataclasite (A) sample 4. Equal area projections and contours in multiples of a random distribution (m.r.d).

3.2.2 Host rocks

3.2.2.1 Siltstone

Siltstones have quartz which is highly fractured and has angular shape, suggesting fraction process. In addition, there are a lot of altered quartz grains, which indicates deformation processes (Figure 3.10A). SEM image show shear surface which crosscut illite, suggesting that siltstone underwent shear history (Figure 3.10B). Fracture and pore is filled by iron oxide solution. The iron-rich clay mineral in these samples (Figure 3.10C) can indicate hydrothermal alteration process. In high magnification, SEM images show the clay mineral flow along quartz grain, suggesting faulting process (Figure 3.10D). Siltstone fabrics are moderate in (001) plane with maxima range of 1.8-2.6 m.r.d. (Figure 3.12). Phase proportion of these samples from Rietveld analysis consists of eight minerals in sample 5 and six minerals in sample 6. They are presented in (Figure 3.11) and summarized in (table 3.1).
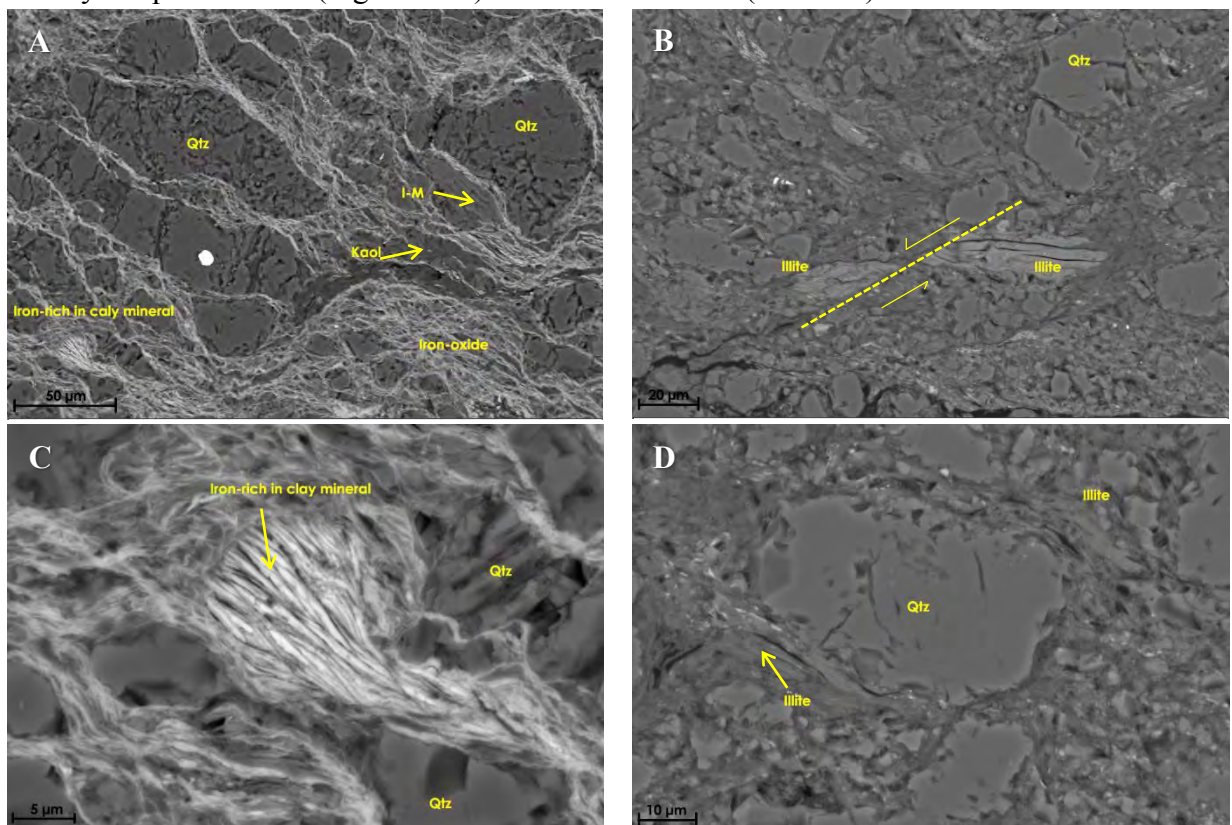
Figure 3.10 SEM-BSE images of siltstone. (A) Deformation and fraction of quartz grain. (B) Shear surface which crosscut illite. (C) Iron-rich clay mineral. (D) Clay mineral flow along quartz grain. Qtz: quartz, I-M: Illite-mica
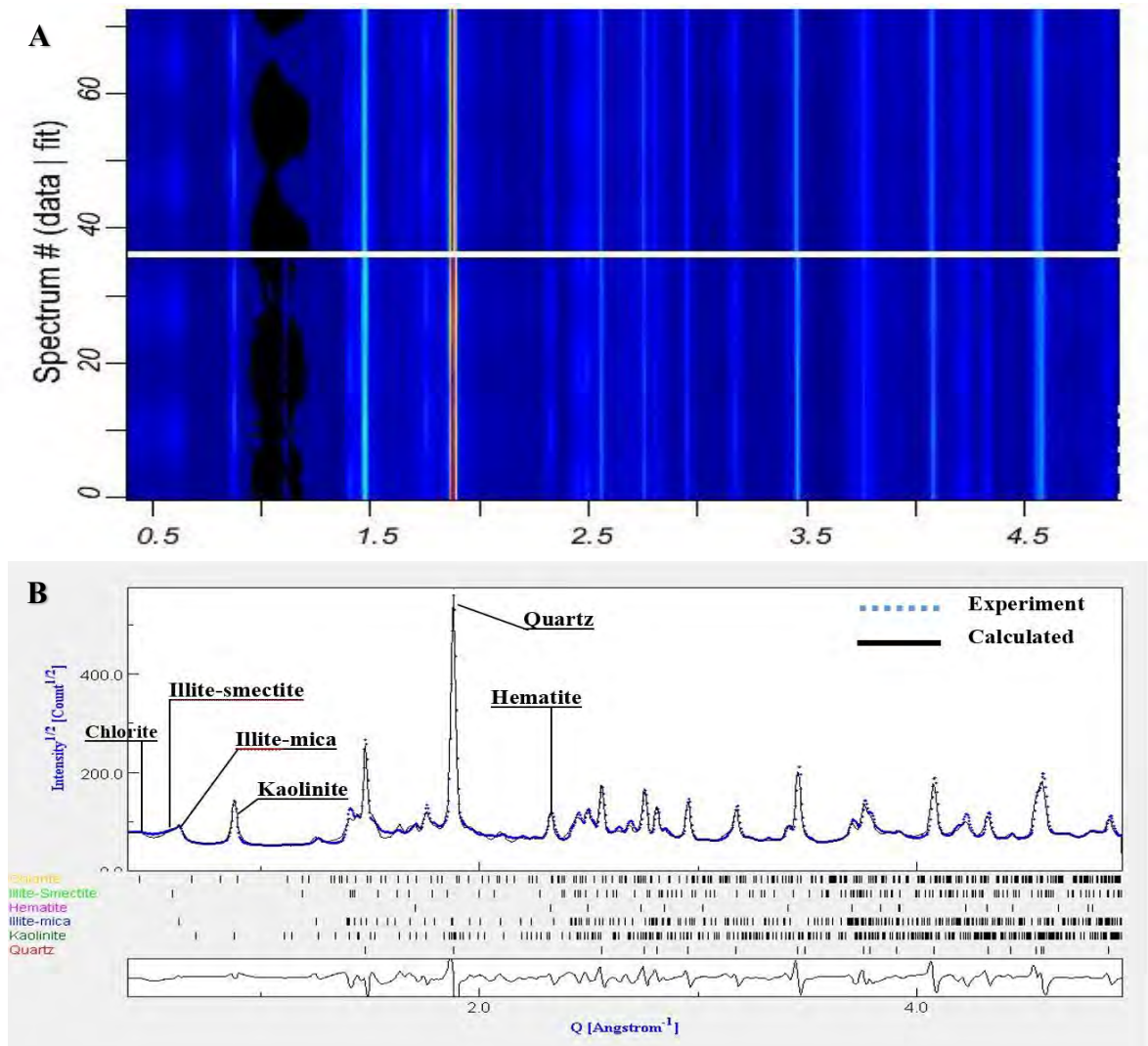
Figure 3.11 Diffraction pattern of siltstone (sample 6). Scale is Q ($2\pi/d$). (A) Stack of 36 diffraction spectra in 2D map plots, comparing experimental data (bottom) with calculated spectra (top) for an image taken at 0° tilt and averaged over 10° azimuthal intervals. (B) Average diffraction spectrum. Blue dots are measurements and black solid line is the Rietveld fit. The peak position of contributing phase is indicated at the bottom.
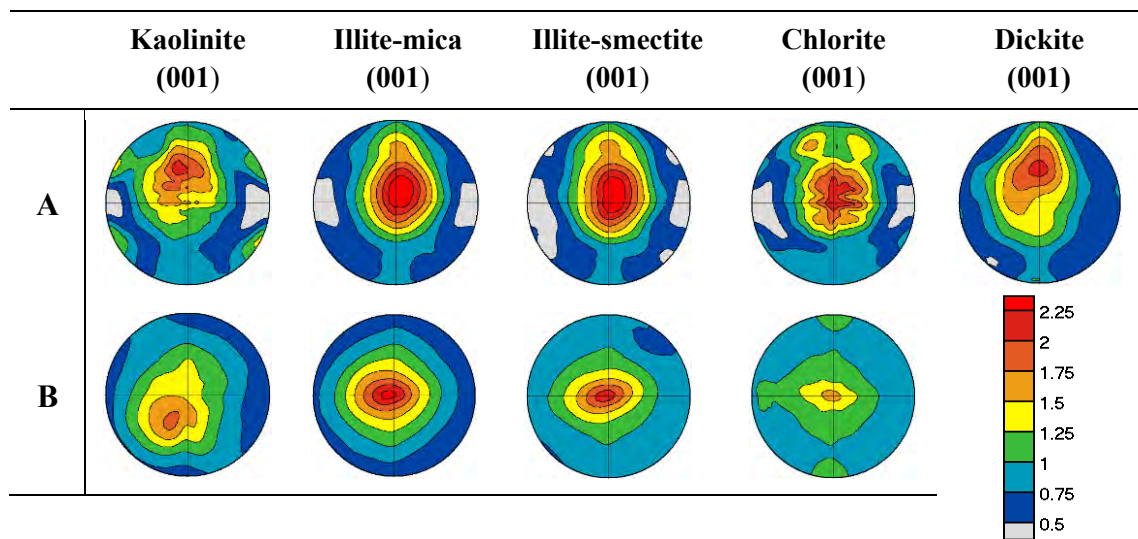
Figure 3.12 (001) pole figures for kaolinite, illite-mica, illite-smectite, cholrite, and dickite of siltstone. (A) # sample 5, (B) # sample 6. Equal area projection, contours in multiples of a random distribution (m.r.d).

3.2.2.2 Shale

SEM images of this sample illustrate microstructure and orientation of phyllosilicate minerals (Figure 3.13A). Pyrite is found in this sample and show well developed framboidal crystal forms (Figure 3.13B). Phase proportion from Rietveld analysis are fairly consistent with the XRD analysis: quartz (42.093 wt%), illite-mica (27.655 wt%), illite-smectite (18.537 wt%), dickite (9.106 wt%), and chlorite (2.609 wt %) (Figure 3.14). All sheet silicates has maximum pole figure perpendicular to the bedding plane (Figure 3.15). Illite-mica display strongest preferred orientation of 3.9 m.r.d. but the weakest is shown in illite-smectite accounting for 2.6 m.r.d.

Figure 3.13 SEM-BSE images of Shale. (A) Microstructure and orientation of phyllosilicate minerals in sample 7. (B) Framboidal crystal forms of pyrite. Qtz: quartz, F: feldspar, Py: pyrite, I-S: Illite-smectite, I-M: Illite-mica
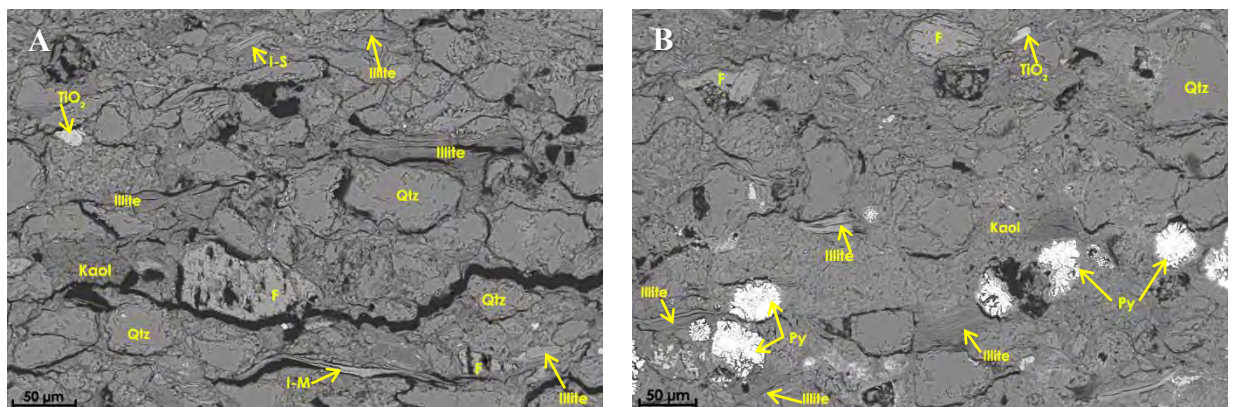
Figure 3.14 Diffraction pattern of siltstone (sample 6). Scale is Q (2π/d). (A) Stack of 36 diffraction spectra in 2D map plots, comparing experimental data (bottom) with calculated spectra (top) for an image taken at 0° tilt and averaged over 10° azimuthal intervals. (B) Average diffraction spectrum. Blue dots are measurements and black solid line is the Rietveld fit. The peak position of contributing phase is indicated at the bottom.
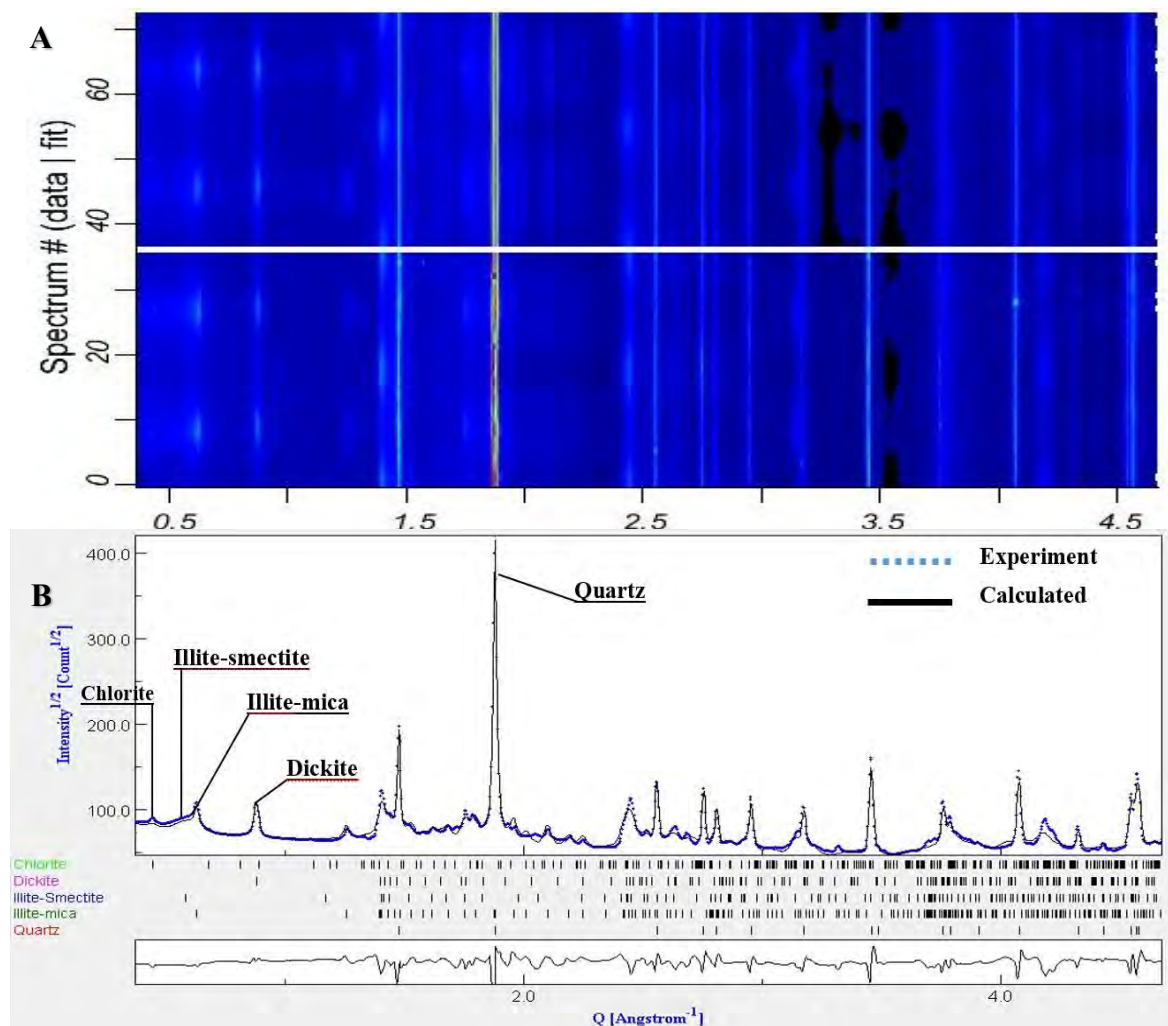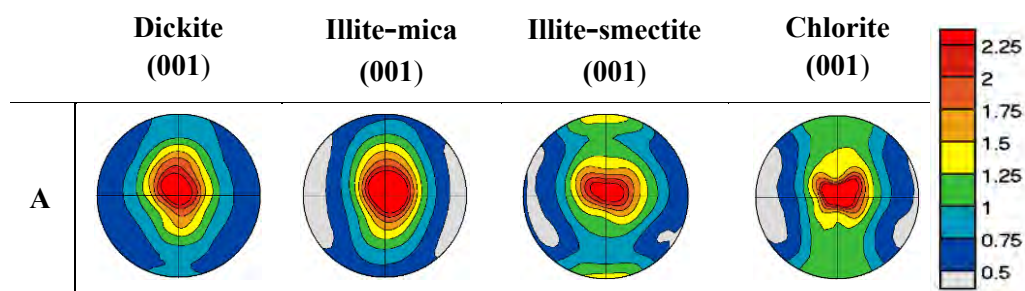

Figure 3.15 (001) pole figures for dickite, illite-mica, illite-smectite, and cholrite, of shale. (A) # sample 7. Equal area projection, contours in multiples of a random distribution (m.r.d).

3.2.2.3 Sandstone

Samples are medium to very fine-grained white sandstone. According to SEM analysis, there is no CPO of clay minerals in the samples. Clay minerals and mica are mostly randomly oriented between angular quartz grain (Figure 3.16A,). The SEM image show deformation of quartz and foldings of illite-mica, indicating that the sandstone underwent fault history (Figure 3.16B). The iron oxide filled between quartz grains and fraction zone (Figure3.16B). In high magnification SEM image shows the layers of iron solution (Figure 3.16C). Titanium dioxide (Figure 3.16D) is also found in this sample. Pore spaces are filled with pyrite that present well developed cubic and framboidal crystal forms. There is no obvious preferred orientation of phyllosilicate minerals. The texture of these samples are weak and display asymmetries on pole figures with CPO ranging from 1.0-1.2 m.r.d. (Figure 3.18) due to weak foliation in both samples. The samples composed of five, seven and six minerals in sample 8 to 10, respectively (Figure 3.17).

Figure 3.16 SEM-BSE images of sandstone. (A) Kaolinite is mostly randomly oriented between quartz grain. (B) Deformation of quartz and fold of Illite-mica (C) The layers of iron solution. (D) Precipitation of Titanium Dioxide. Qtz: quartz, Kaol: kaolinite, I-M: Illite-mica
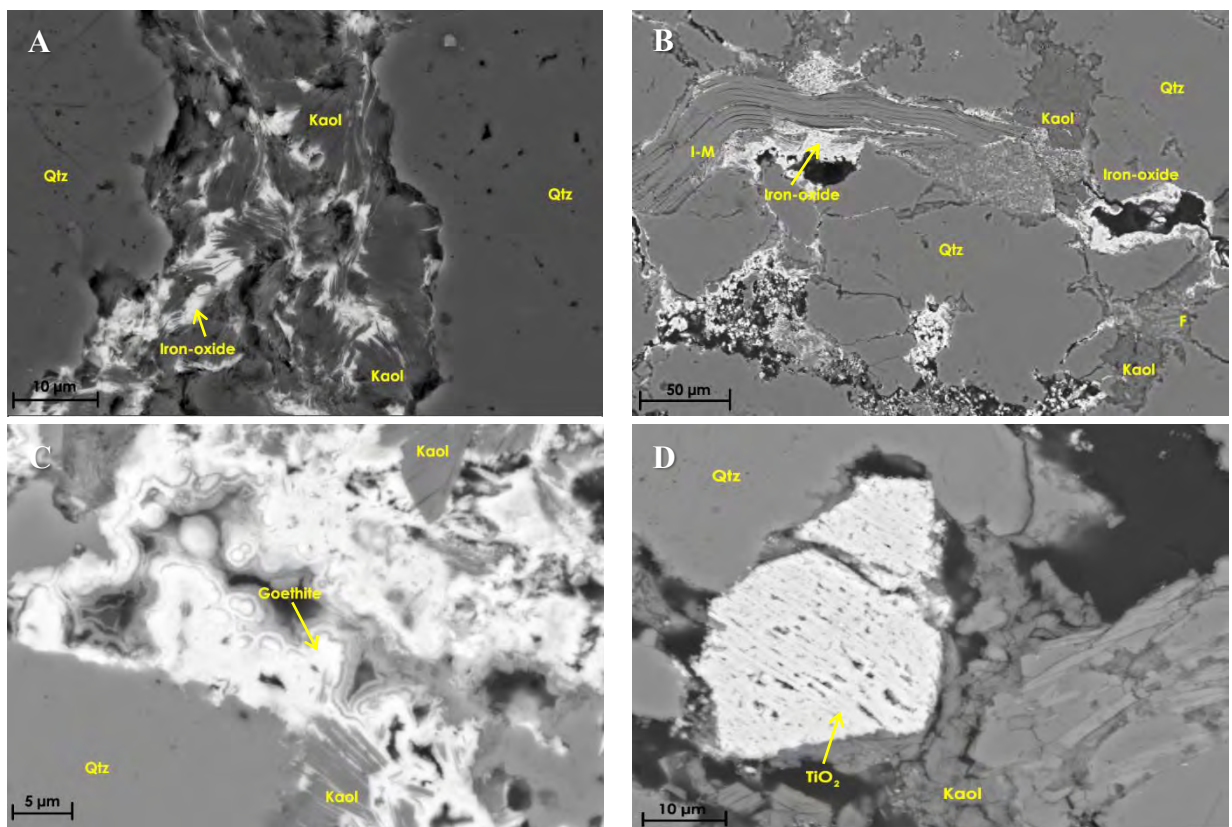
Figure 3.17 Diffraction pattern of sandstone (sample 9). Scale is Q ($2\pi/d$). (A) Stack of 36 diffraction spectra in 2D map plots, comparing experimental data (bottom) with calculated spectra (top) for an image taken at 0° tilt and averaged over 10° azimuthal intervals. (B) Average diffraction spectrum. Blue dots are measurements and black solid line is the Rietveld fit. The peak position of contributing phase is indicated at the bottom.
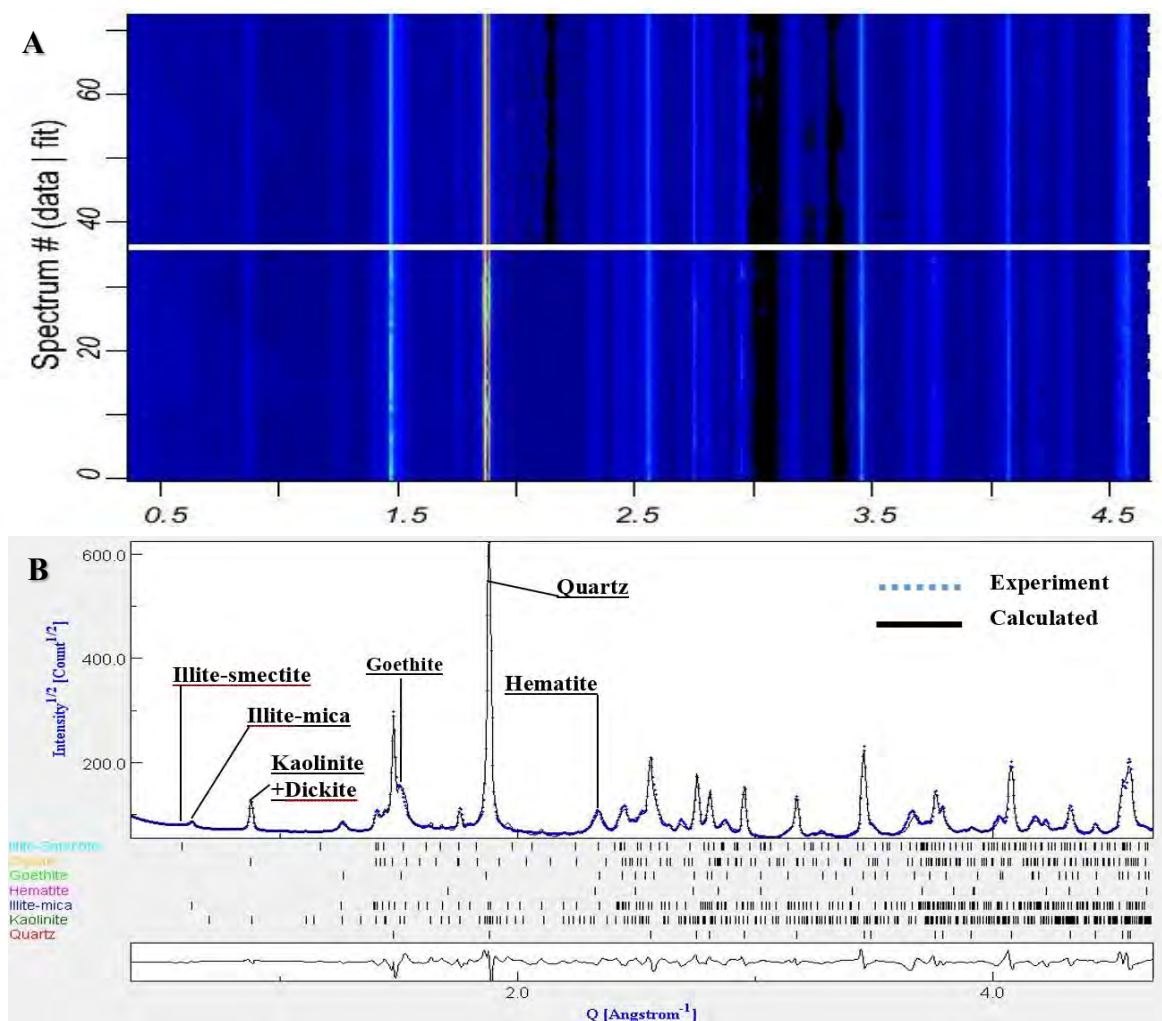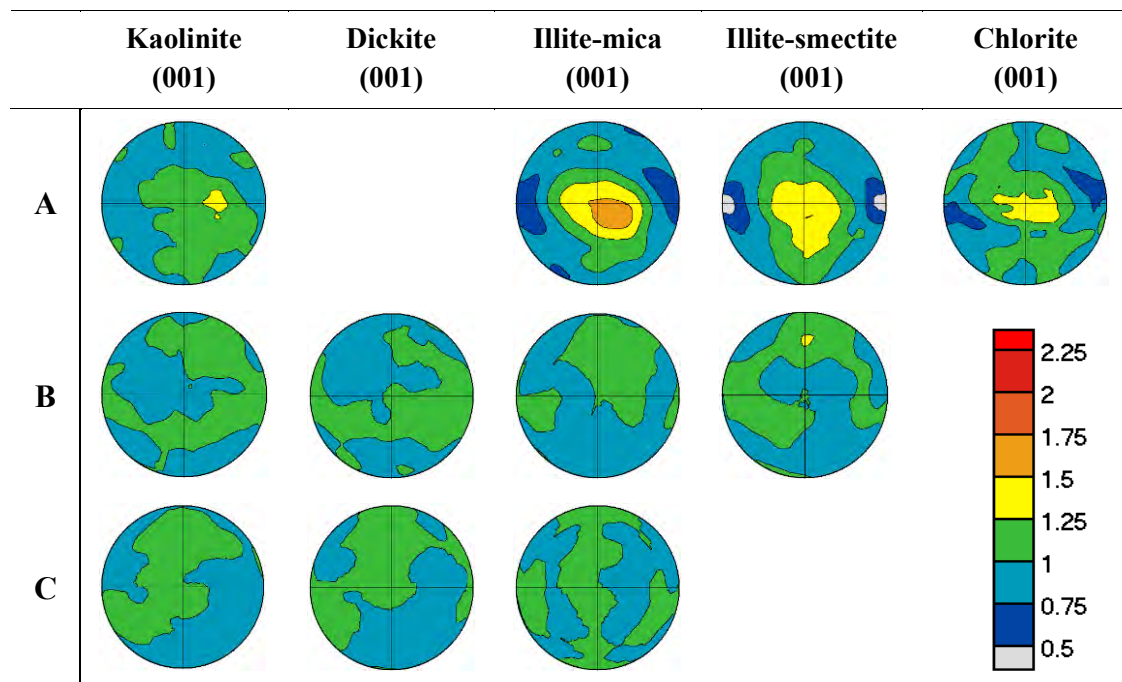
Figure 3.18 (001) pole figures for kaolinite, dickite, illite-mica, illite-smectite, and cholrite of sandstone. (A) # sample 8, (B) # sample 9, (C) # sample 10. Equal area projection, contours in multiples of a random distribution (m.r.d).

Chapter 4: Discussion

4.1 Microstructure

4.1.1 Deformation

4.1.1.1 Fraction of quartz

4.1.1.2 Fold of phyllosilicate

4.1.2 Hydrothermal alteration

4.2 Fault gouge fabric

4.2.1 Comparison between fault gouges and host rocks

4.2.2 Comparison with the other studies

4.3 Amorphous material

4.4 Heavy mineral

4.4.1 Hollandite

4.4.2 Anatase

4.1 Microstructure

4.1.1 Deformation

Faulting produced altered quartz grains, folded phyllosilicate mineral, and distinct shear zones.

4.1.1.1 Fraction of quartz

SEM images of all samples, especially the rock from fault zone illustrate the fraction and deformation of quartz grain, suggesting that those samples were forced by faulting process. That process causes a decrease in grain size and sometimes a deterioration of sorting (Engelder, 1974), which lead to cataclasite or fault gouge.

4.1.1.2 Fold of phyllosilicate mineral

Folded and kinked sheet silicate are disseminated in whole matrix. In addition, some phyllosilicate folds and wraps other clasts such as quartz or feldspar. That behavior of phyllosilicate results from the fact that sheet silicate was forced by faulting process, which causes the mineral to break contributing to newly form in edge-to-face contact (Janssen *et al.*, 2012) as clay-clast aggregates (CAAs) (Boutareaud *et al.*, 2010)

4.1.1.3 Shear zone

SEM images illustrate shear line which crosscuts illite in sample 6 and illite shows the foliated gouge along shear area in sample 3, suggesting microtectonics in local zone which lead to deformation process.
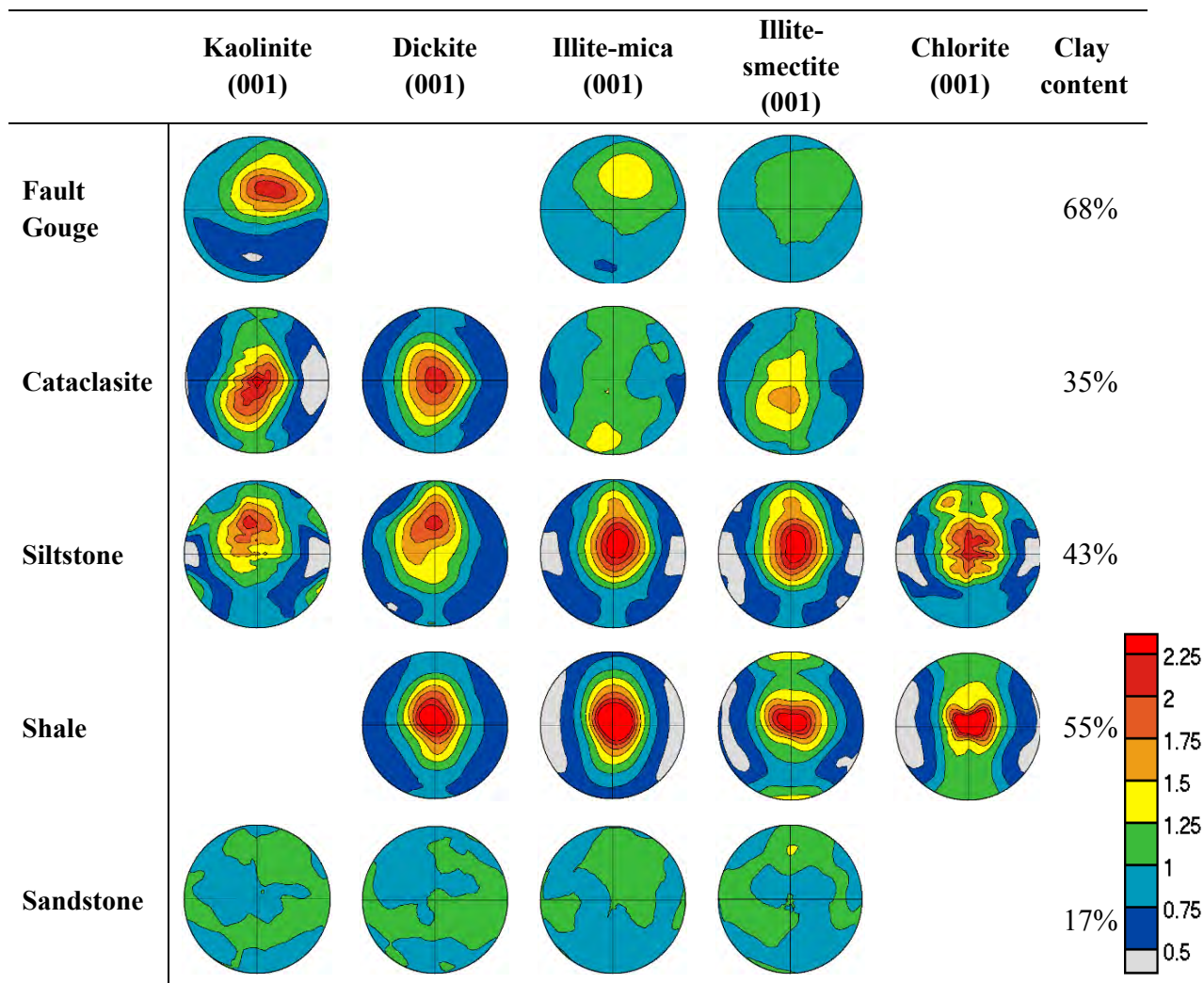
4.1.2 Hydrothermal alteration

Hydrothermal alteration is one of the reasons that causes physical and chemical conditions of mineral alter. For example, kaolinite produced by the chemical weathering of aluminum silicate minerals like feldspar (Shelton, 1904) , which contributes to high clay content in fault gouge. Goethite and hematite, which are iron-baring mineral, were found both in fracture and pore in all samples. They are also a precipitation in hydrothermal fluids which indicates that the minerals in this study area were altered by hydrothermal process.

4.2 Fault gouge fabric

4.2.1 Comparison between fault gouges and host rocks

Normally, the rocks with high clay content have crystallographic preferred orientation of clay minerals more than the rocks with low clay content. On the other hand, fault gouges have high clay content more than other rocks but they have weak preferred orientation compared with shale and siltstone. The cause comes from the fact that those rocks were deformed by faulting process and altered by hydrothermal alteration process. Those processes contribute to fraction of sheet silicate and alteration of some minerals such as feldspar or mica, which lead to high clay content. By contrast, those processes result in fault gouge fabrics are weak and asymmetric (Figure 4.1).

|	Kaolinite (001)	Dickite (001)	Illite-mica (001)	Illite-smectite (001)	Chlorite (001)	Clay content
Fault Gouge						68%
Cataclasite						35%
Siltstone						43%
Shale						55%
Sandstone						17%

Figure 4.1 (001) pole figures for kaolinite, dickite, illite-mica, illite-smectite, and chlorite of the sample from 5 groups. Equal area projection, contours in multiples of a random distribution (m.r.d).

4.2.2 Comparison with the other studies

Texture of fault gouges is weak and asymmetric (Haines *et al.,* 2009; Wenk *et al.,* 2010; Buatier *et al.,* 2012; Janssen *et al.,* 2012). The study of Haines *et al.* describes clay fabric maxima between 1.7-4 m.r.d. and that of Wenk *et al.* in San Andreas fault, Buatier *et al.* in Bogd fault, and Janssen *et al* in San Andreas fault explain texture of clay mineral maxima in range of 1.5-2.5 m.r.d., 13.2.6 m.r.d., and around 1.2 m.r.d. respectively. These agree with my samples because overall, my fault gouge fabrics are weak and asymmetric with maxima on (001) in range of 1.2 m.r.d. in Illite-smectite to 2.4 m.r.d. in Kaolinite.

4.3 Amorphous material

Based on amorphous material, it cannot conclude that what the amorphous material comes from. Compared with the study of Janssen *et al.*,2010 and Janssen *et al.*,2014, Amorphous material may result from two main mechanisms: friction melting (Sibson,1975) or comminution of clasts (crush-origin pseudotachylytes) (Wenk,1978) (Figure 4.2). To have a better understanding of amorphous material, it is required to study in high resolution in order to understand the accumulation pattern of amorphous material.
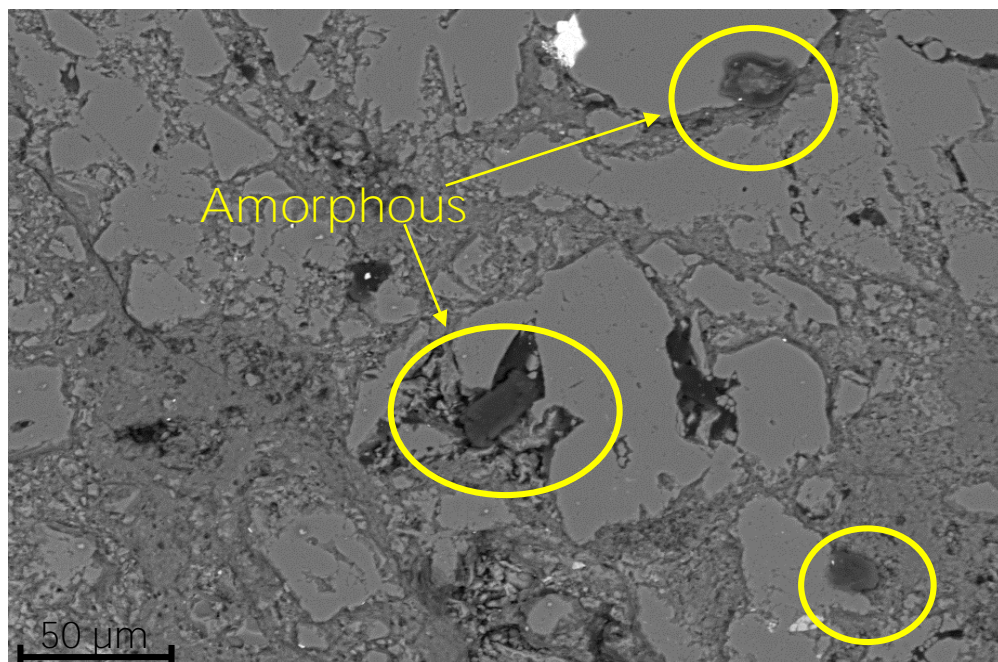
Figure 4.2 SEM-BSE images of amorphous materials in fault gouge in sample 1

4.4 Heavy mineral

4.4.1 Hollandite

Hollandite was found in all sample which is from fault zone. There are several occurrence of hollandite such as a primary mineral in contact metamorphic manganese ores or secondary weathering product of earlier manganese-bearing minerals (Biagioni *et al.*, 2012). In this case, the occurrence of hollandite may result from secondary weathering product of earlier manganese-bearing minerals because igneous rock (intrusive rock) was not found in the study area. Thus, this mineral does not result from contact metamorphic.

4.4.2 Anatase

Anatase was found in all sample. Anatase is one of titanium dioxide which occurs in natural. Compared with rutile considered to be the high-temperature and high-pressure, anatase prefers to occur in low pressure (Dachilleetal *et al.*, 1968). It results from the weathering of other titanium-bearing minerals and deposit from hydrothermal solution (Bishop *et al.*, 1999), which supports the hydrothermal alteration in this area.

Chapter 5: Conclusion

We observe several deformation textures, such as fractured quartz and folding and kinking band in phyllosilicate minerals, in both fault gouges and adjacent host rocks. These characteristics indicate the deformation from intense faulting process. In addition, minor hydrothermal alterlation spots are detected as indicated by the present of goethite. In general, higher clay-content rock tends to have stronger crystallographic preferred rorientation. Nevertheless, in this area, shales (55% wt clay) is stronger oriented (i.e. higher m.r.d.) than fault gouges (68% wt clay). This strange behavior results from a localized shear stress from faulting process and secondary alteration from hydrothermal.

REFERENCE

Bishop, A., Woolley, A., and Hamilton, W. Cambridge Guide to Minerals, Rocks and Fossils. 2nd ed. Natural History Museum (London, England), 52.

Biagioni, C., Capalbo C., and Pasero M. Nomenclature tunings in the hollandite supergroup European Journal of Mineral., 25 (2013), 85–90

Boutareaud, S., Boullier, A.-M., Andreani, M., Calugaru, D.-G., Beck, P., Song, S.-R., and Shimamato, D.-G. Clay clast aggregates: new textural evidence for seismic faulting. Journal of Geophysical Research, 2010(115).

Buatier, M., Chauvet, A., Kanitpanyacharoen, W., Wenk, H., Ritz, J., and Jolivet, M. (n.d.). Origin and behavior of clay minerals in the Bogd fault gouge, Mongolia. Journal of Structural Geology, 2012(34), 77-90.

Cooper, M. A., Herbert, R., and Hill, G. S. The structural evolution of Triassic intermountain basins in Northeastern Thailand T. Thanasuthipitak (Ed.), Proceedings of the International Symposium on Intermountain Basins: Geology and Resources, Chiang Mai (1989), 153–184

Davis, G. H., and Reynolds, R. J. Structural geology of rocks and regions. 2nd ed. New York: John Wiley & Sons, Inc., 1996, 776.

Dacchille, F., Simons. P. Y., and Roy, R. Pressure-Temperature studies of anatase, brookite, rutile and TiO_2-II. The American mineralogist, 1968(53)

DMR, Geologic map of Changwat Phetchcun [Online]. 2009. Source: http://www.dmr.go.th/download/pdf/North/Petchaboon.pdf [7 May 2016]

Engelder, J. T. Cataclasis and the generation of fault gouge: Geological Society of America Bulletin, 1974(85), 1515-1522

Haines, S.H., van der Pluijm, B.A., Ikari, M.J., Saffer, D.M., and Marone, C. Clay fabric intensity in natural and artificial fault gouges: implications for brittle fault zone processes and sedimentary basin clay fabric evolution. Journal of Geophysical Research, 2009(114). http://dx.doi.org/10.1029/2008JB005866.

Janssen, C., Wirth, R., Rybacki, E., Kienast, M., Wenk, H.-R., and Dresen, G. Amorphous material in SAFOD core samples (San Andreas Fault): Evidence for crush-origin pseudotachylytes? Geophysical research letters, 2010(37).

Janssen, C., Wirth, R., Reinicke, A., Rybacki, E., Naumann, R., Kemmnitz, H., Wenk, H.-R., and Dresen, G. Nanoscale porosity in SAFOD core samples (San Andreas fault). Earth and Planetary Science Letters 301, 2011, 179e189.

Janssen, C., Kanitpanyacharoen, W., Wenk, H., Wirth, R., Rybacki, E., Kienast, M., and Dresen, G. Clay fabrics in SAFOD core samples. Journal of Structural Geology, 2012(43), 118-127.

Janssen, C., Wirth, R., Wenk, H., Morales, L., Naumann, R., Kienast, M., Song, S., and Dresen, G. Faulting processes in active faults e Evidences from TCDP and SAFOD. Journal of Structural Geology, 2014(65), 100-116.

Kanitpanyacharoen, W., Kets, F.B., Wenk, H.-R. and Wirth, R. Mineral Preferred orientation and microstructure of Posidonia Shale in relation to different degrees of thermal maturity. Clays Clay Min., 2012(60), 315-329.

Kanitpanyacharoen, W., Kets, F.B., Wenk, H.-R., Lehr, C., and Wirth, R. Texture and anisotropy of Qusaiba Shales, Saudi Arabia. *Geophys. Pros.,* 2011(59),536-556.

Lutterotti, L., Matthies, S., Wenk, H.-R., Schultz, A.J., and Richardson J.W. Combined texture and structure analysis of deformed limestone from time-of-flight neutron diffraction spectra. Journal of Applied Physics, 1997(81), 594–600.

Morrow, C., Moore, D., and Lockner, D. (n.d.). The effect of mineral bond strength and adsorbed water on fault gouge frictional strength. Geophysical Research Letters, 2000(6), 815-818.

Matthies, S., and Vinel, G. W. On the reproduction of the orientation distribution function of textured samples from reduced pole Figures using the concept of conditional ghost correction. Physica Status Solidi, B112, 1982, K111–K114.

Rietveld, H.M. A profile refinement method for nuclear and magnetic structures. Journal of Applied Crystallography, 1969(2), 65–71.

Sattayarak, N. Review on Geology of Khorat Plateau: In: Proc. of Conf. on Geol. and Min. Resour.of the NE, Thailand, Khon Kaen,1985, 23-30 (in Thai).

Shelton, J. W. Authigenic kaolinite in sandstone. Journal of Sedimentary Petrology, 1964(34), 102-111.

Sibson, R. H. Generation of pseudotachylite by ancient seismic faulting, Geophysics. J. R. Astron. Soc., 1975(43), 775– 794.

Solum, J., Davatzes, N., and Lockner, D. (n.d.). Fault-related clay authigenesis along the Moab Fault: Implications for calculations of fault rock composition and mechanical and hydrologic fault zone properties. Journal of Structural Geology, 2010(32), 1899-1911.

Wenk, H.-R., Lonardelli I., Franz H., Nihei, K., and Nakagawa, S. Preferred orientation and elastic anisotropy of illite-rich shale. Geophysics, 2007(72), E69–E75

Wenk, H. R. Are pseudotachylites products of fracture of fusion? Geology, 1978(6), 507 –511, doi:10.1130/0091-7613(1978)6<507: APPOFO>2.0.CO;2.

Wenk, H., Kanitpanyacharoen, W., and Voltolini, M. (n.d.). Preferred orientation of phyllosilicates: Comparison of fault gouge, shale and schist. Journal of Structural Geology, 2010(32), 478-489.

Vrolijk, P., and van der Pluijm, B.A., 1999. Clay gouge. Journal of Structural Geology 21, 1039e1048.

APPENDIX

MAUD Analysis of All Samples

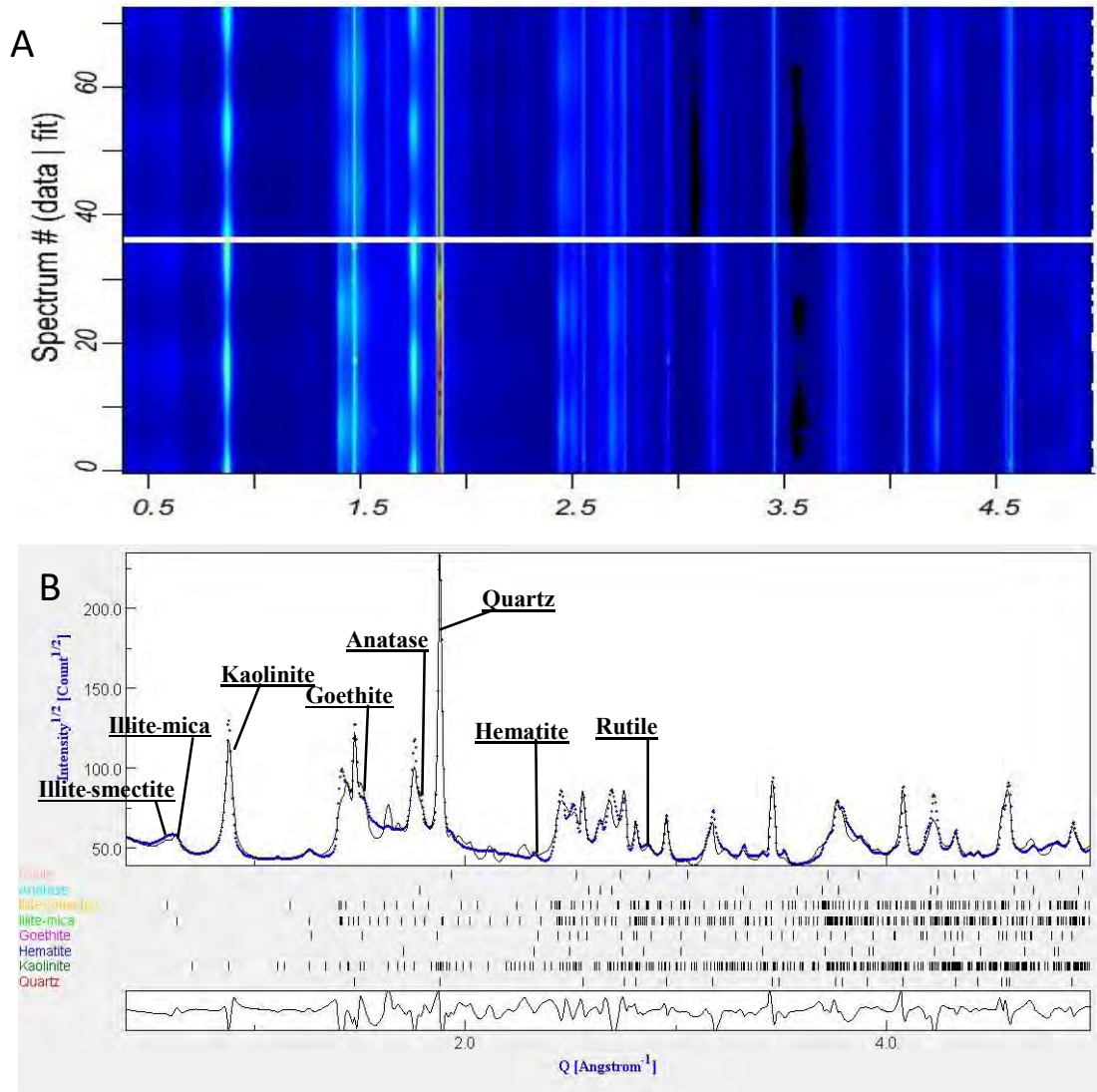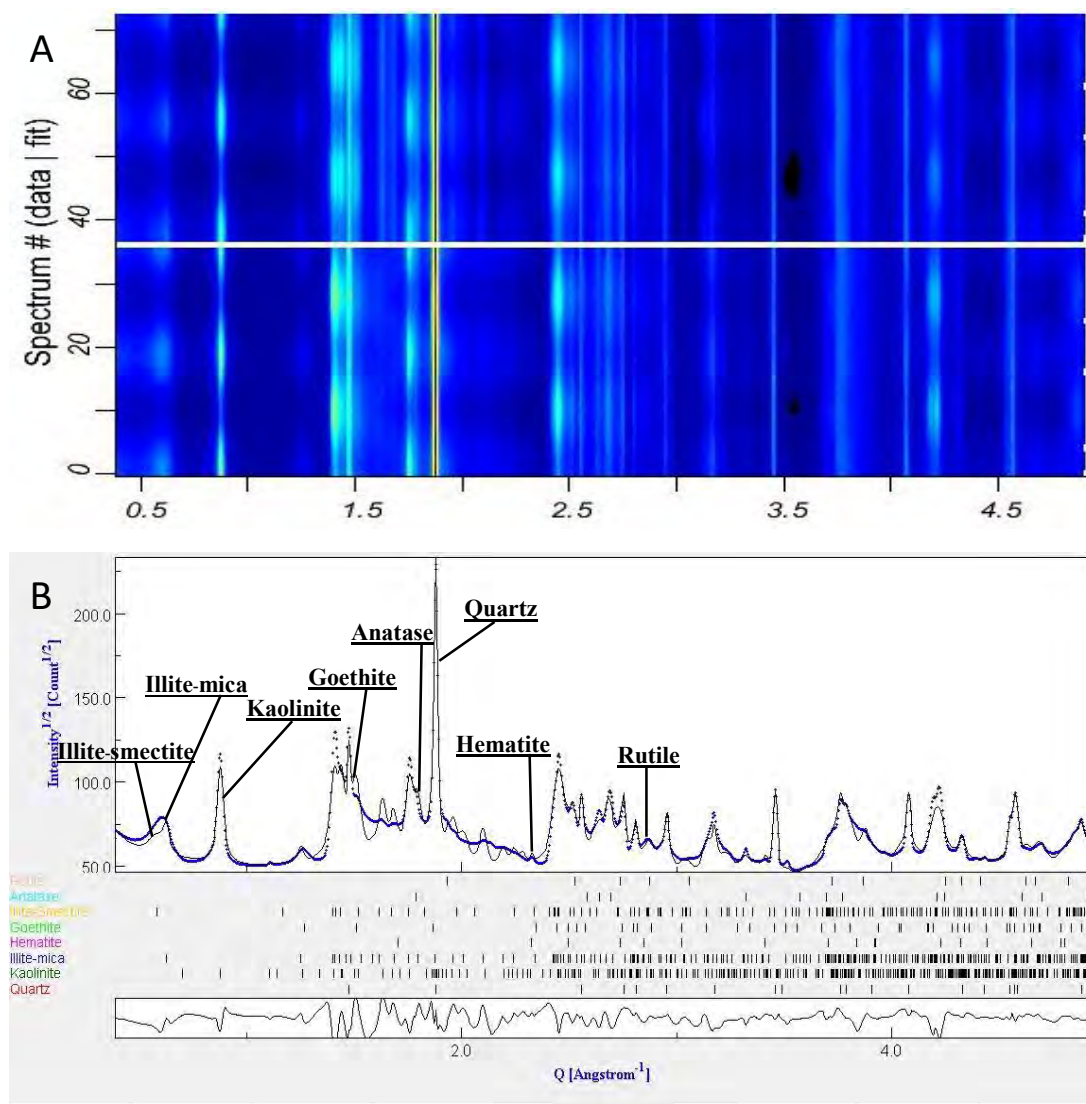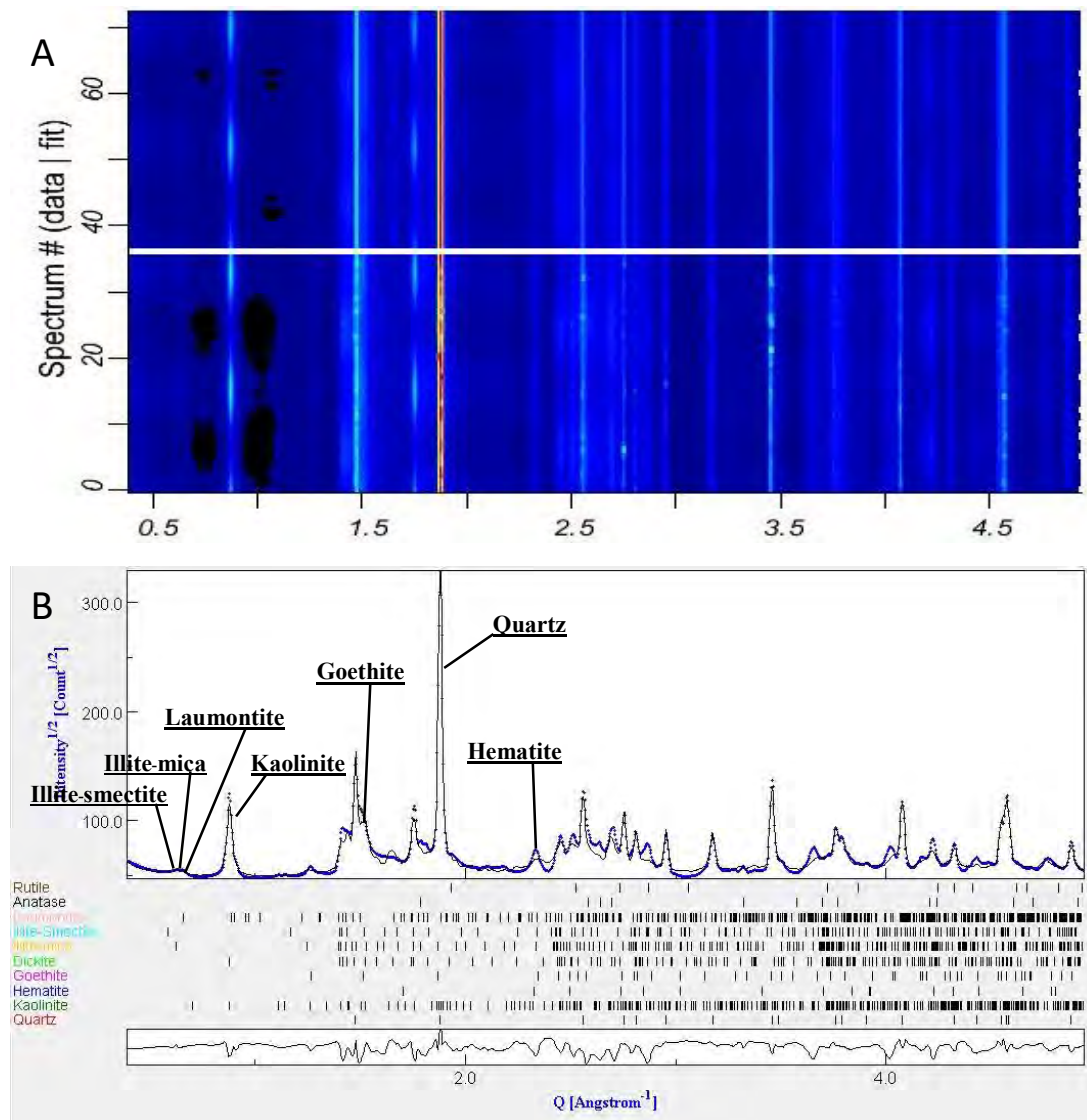<u>Sample 1</u>
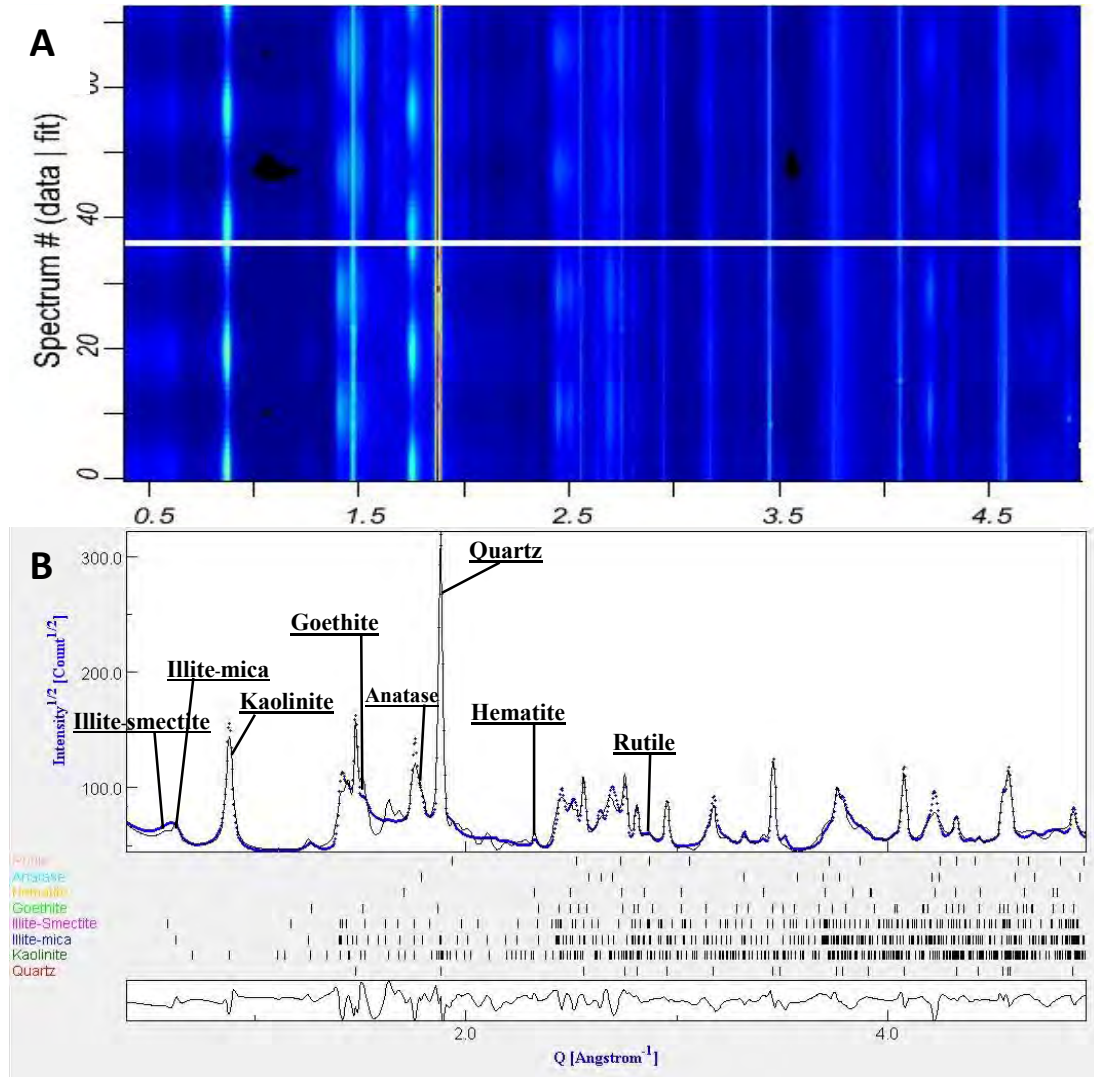
A.1 Diffraction patterns of fault gouges (sample 1). Scale is Q ($2\pi/d$). (A) Stack of 36 diffraction spectra in 2D map plots, comparing experimental data (bottom) with calculated spectra (top) for an image taken at 0∘ tilt and averaged over 10∘ azimuthal intervals. (B) Average diffraction spectrum. Blue dots are measurements and black solid line is the Rietveld fit. The peak position of contributing phase is indicated at the bottom.
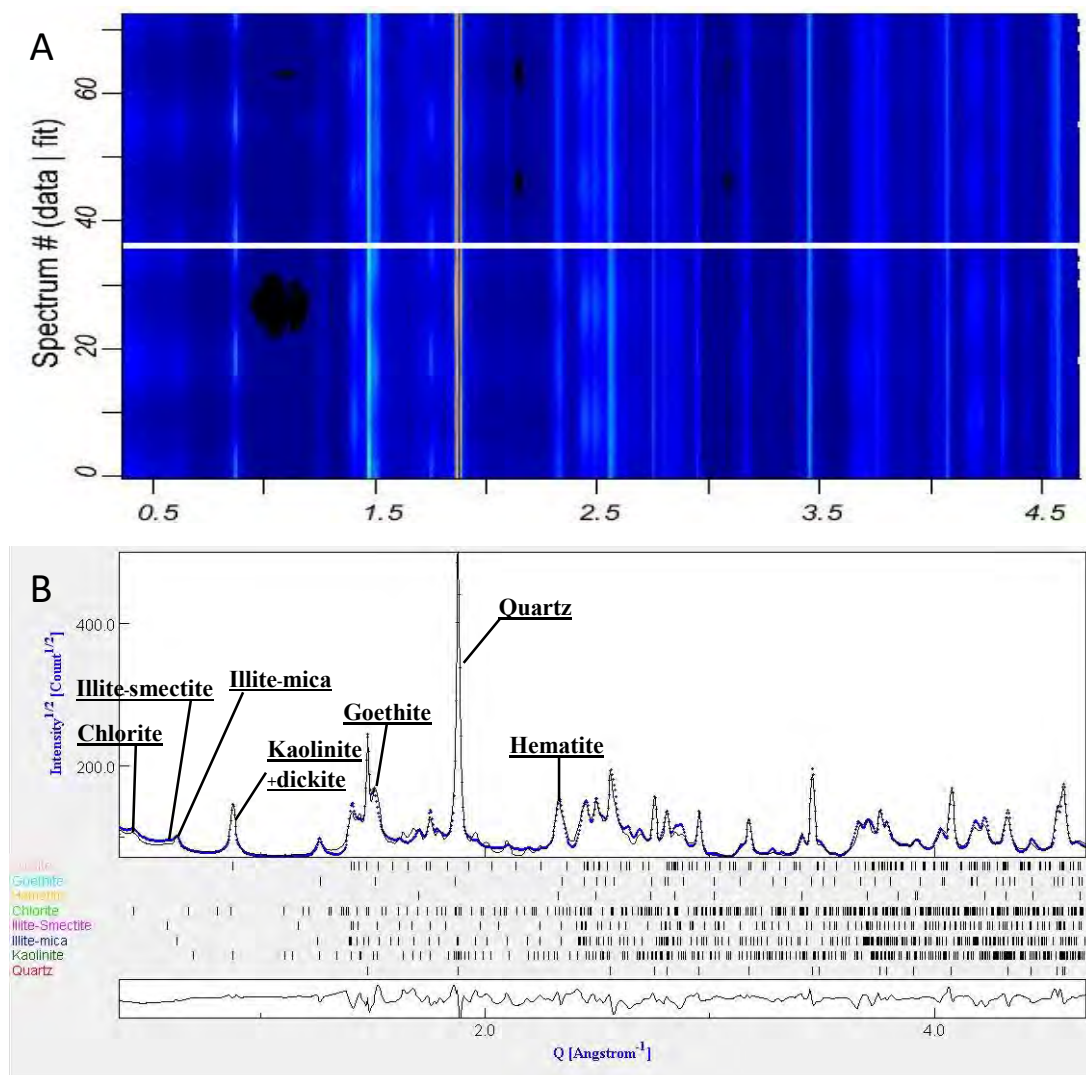
Sample 2

A.2 Diffraction patterns of fault gouges (sample 2). Scale is Q (2π/d). (A) Stack of 36 diffraction spectra in 2D map plots, comparing experimental data (bottom) with calculated spectra (top) for an image taken at 0∘ tilt and averaged over 10∘ azimuthal intervals. (B) Average diffraction spectrum. Blue dots are measurements and black solid line is the Rietveld fit. The peak position of contributing phase is indicated at the bottom.

Sample 3

A.3 Diffraction patterns of fault gouges (sample 3). Scale is Q (2π/d). (A) Stack of 36 diffraction spectra in 2D map plots, comparing experimental data (bottom) with calculated spectra (top) for an image taken at 0∘ tilt and averaged over 10∘ azimuthal intervals. (B) Average diffraction spectrum. Blue dots are measurements and black solid line is the Rietveld fit. The peak position of contributing phase is indicated at the bottom.
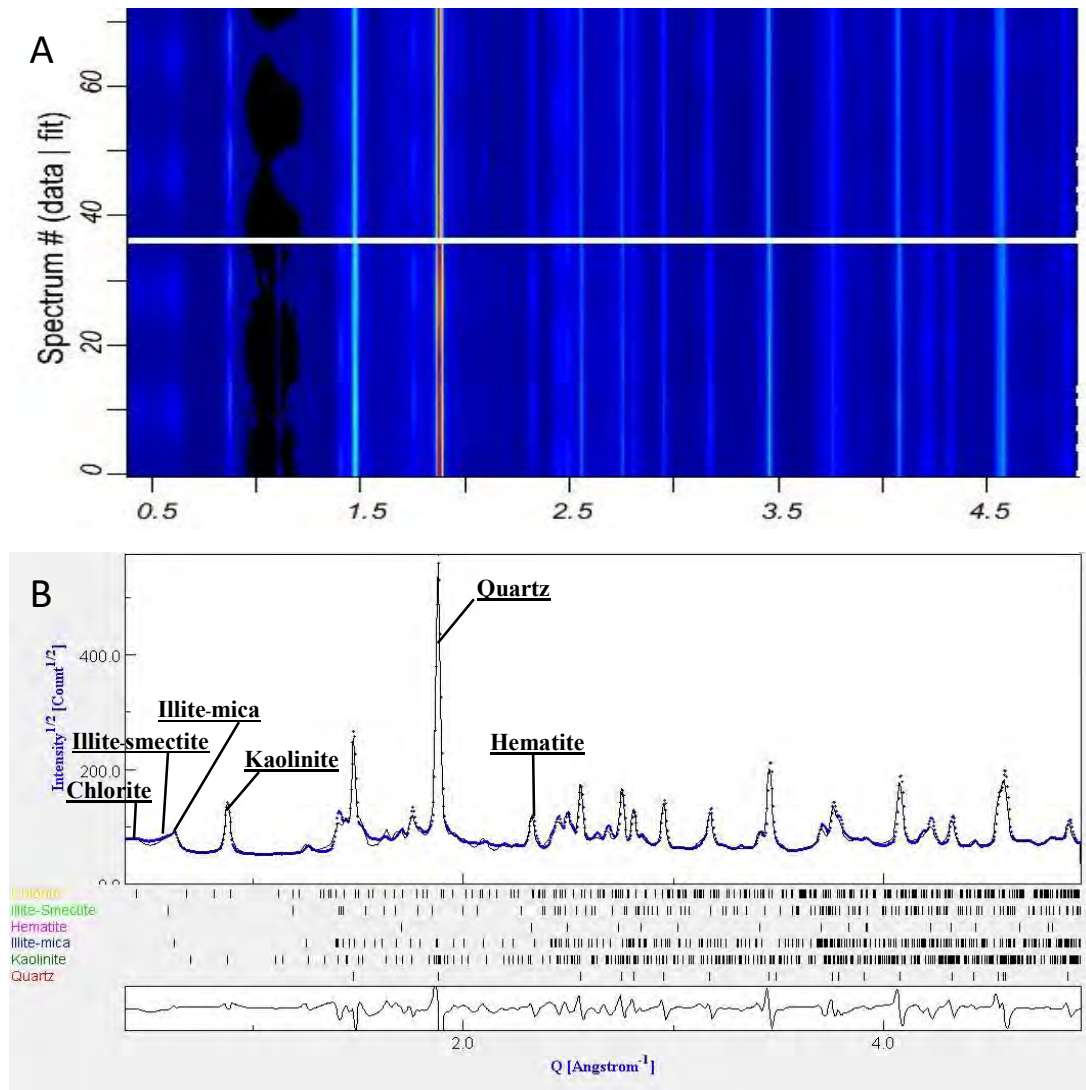
Sample 4

A.4 Diffraction patterns of cataclasite (sample 2). Scale is Q ($2\pi/d$). (A) Stack of 36 diffraction spectra in 2D map plots, comparing experimental data (bottom) with calculated spectra (top) for an image taken at $0\circ$ tilt and averaged over $10\circ$ azimuthal intervals. (B) Average diffraction spectrum. Blue dots are measurements and black solid line is the Rietveld fit. The peak position of contributing phase is indicated at the bottom.
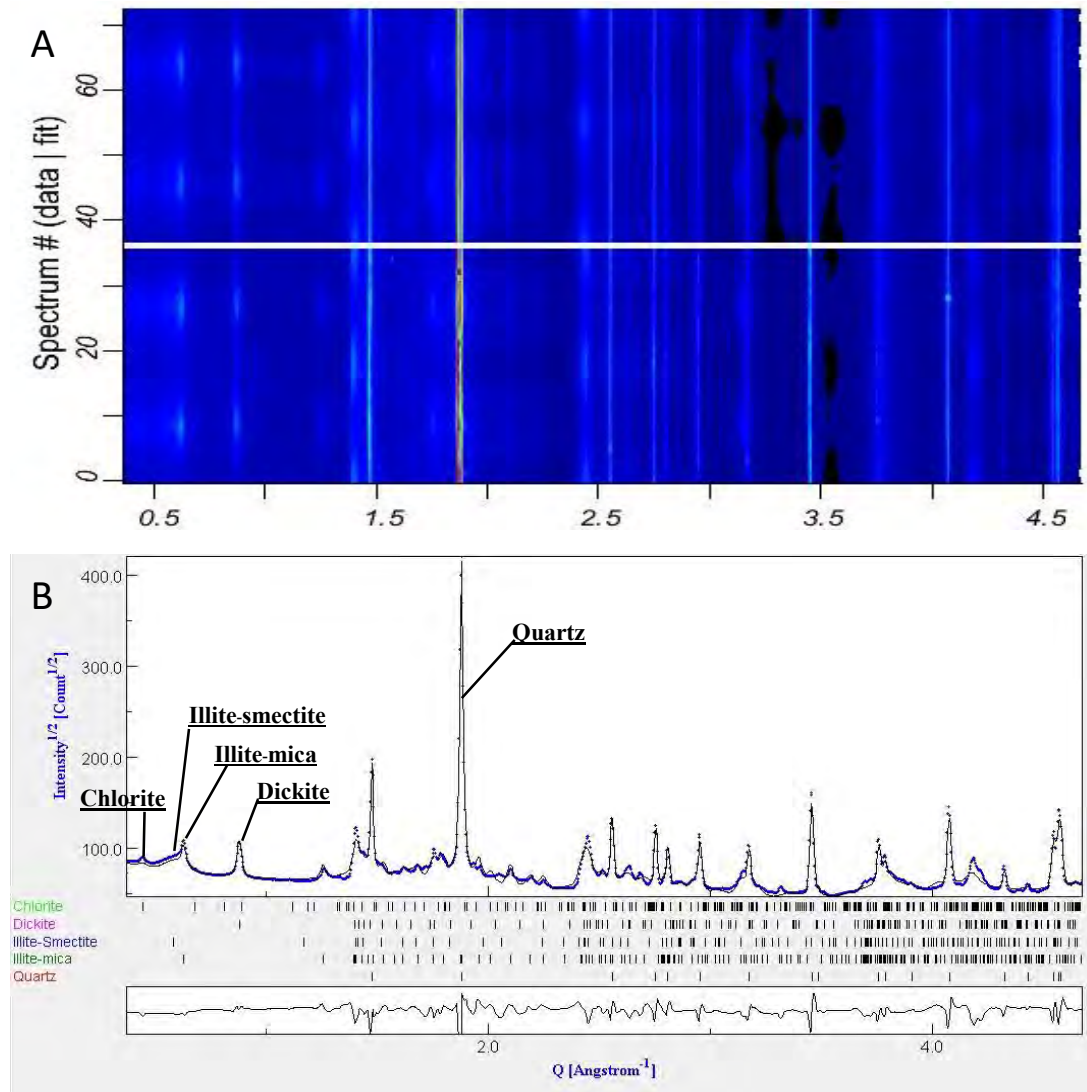
Sample 5

A.5 Diffraction patterns of siltstone (sample 5). Scale is Q ($2\pi/d$). (A) Stack of 36 diffraction spectra in 2D map plots, comparing experimental data (bottom) with calculated spectra (top) for an image taken at 0∘ tilt and averaged over 10∘ azimuthal intervals. (B) Average diffraction spectrum. Blue dots are measurements and black solid line is the Rietveld fit. The peak position of contributing phase is indicated at the bottom.
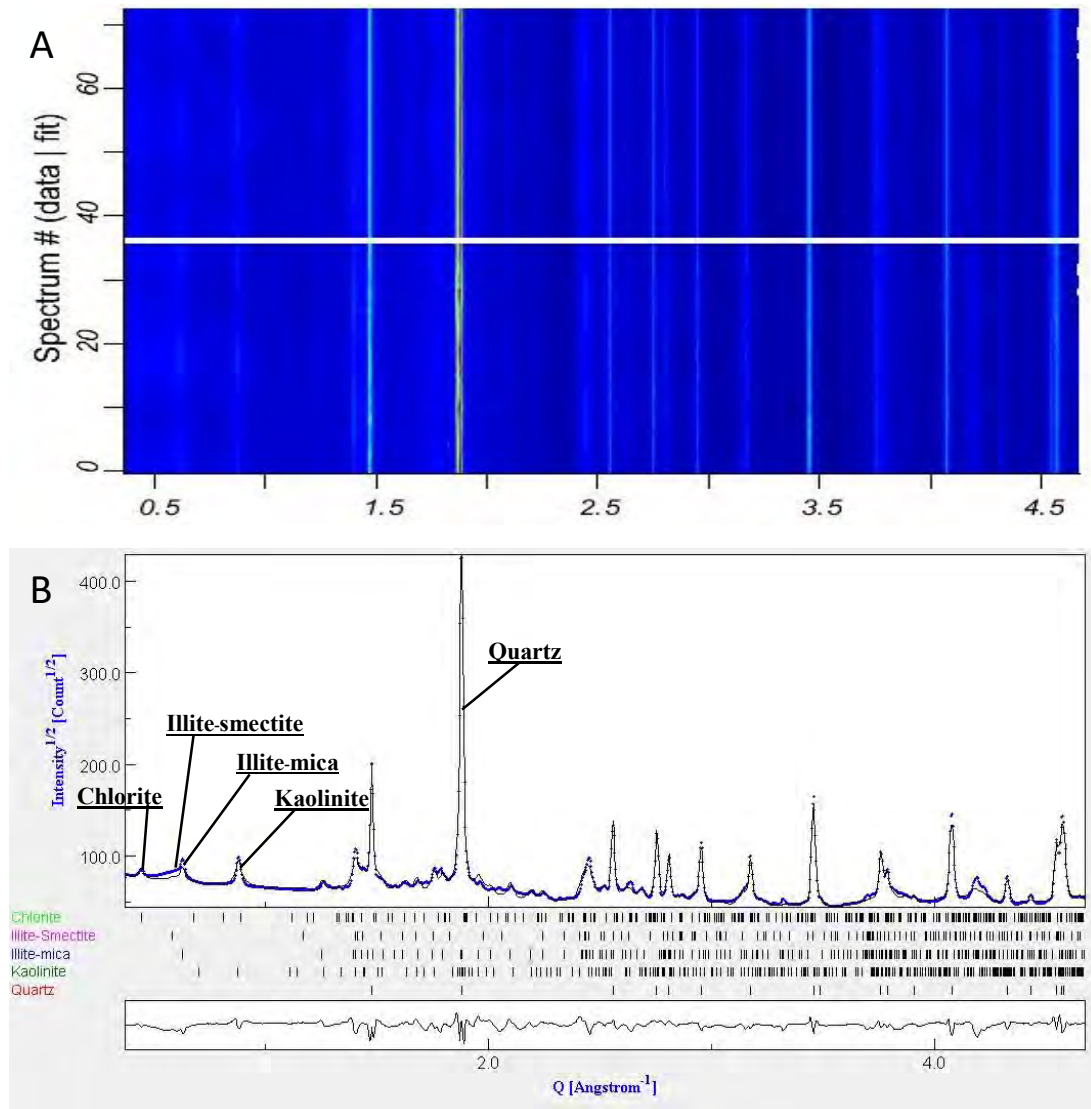
Sample 6

A. 6 Diffraction patterns of siltstone (sample 6). Scale is Q (2π/d). (A) Stack of 36 diffraction spectra in 2D map plots, comparing experimental data (bottom) with calculated spectra (top) for an image taken at 0∘ tilt and averaged over 10∘ azimuthal intervals. (B) Average diffraction spectrum. Blue dots are measurements and black solid line is the Rietveld fit. The peak position of contributing phase is indicated at the bottom.
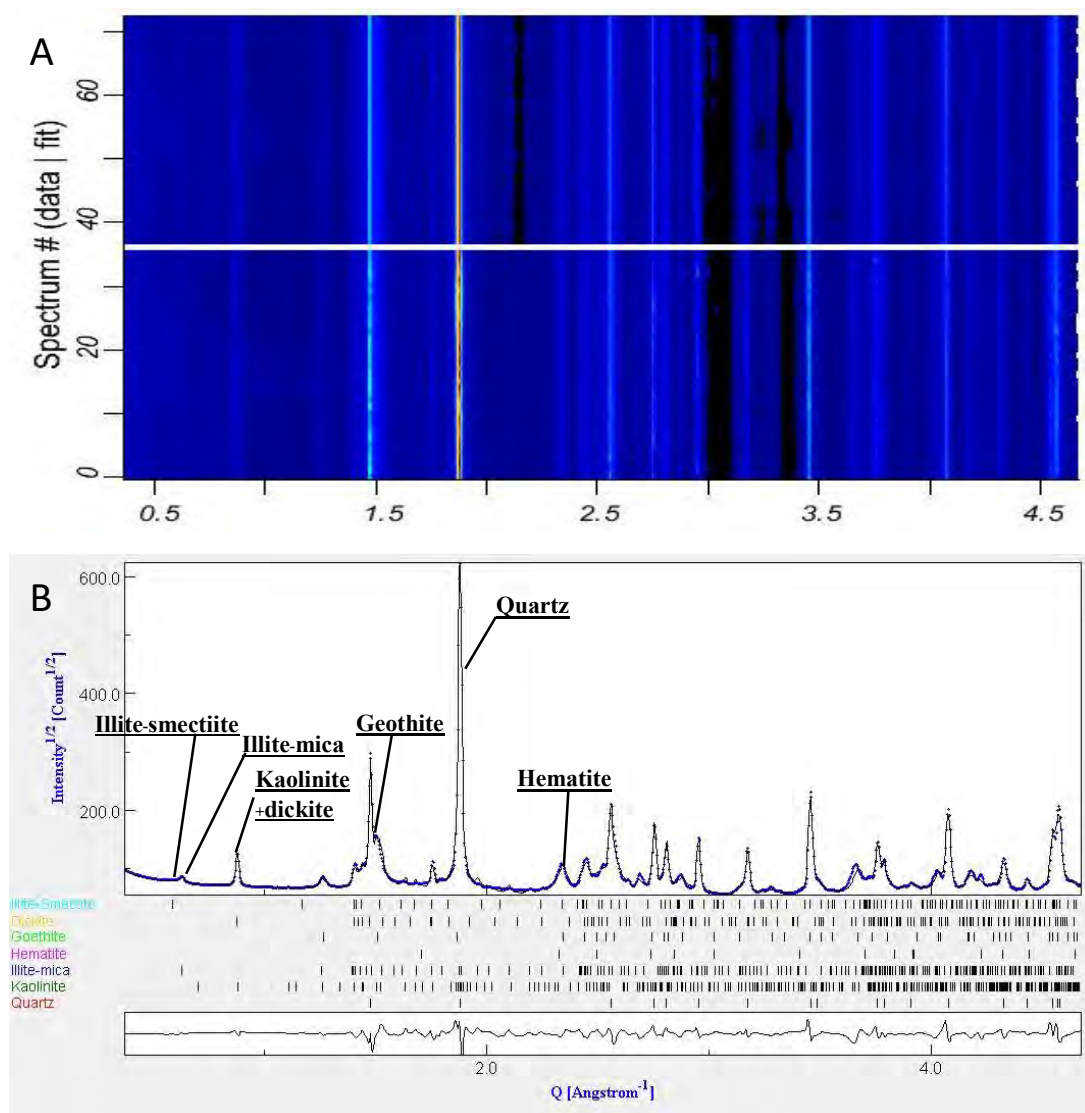
Sample 7

A.7 Diffraction patterns of shale (sample 7). Scale is Q (2π/d). (A) Stack of 36 diffraction spectra in 2D map plots, comparing experimental data (bottom) with calculated spectra (top) for an image taken at 0∘ tilt and averaged over 10∘ azimuthal intervals. (B) Average diffraction spectrum. Blue dots are measurements and black solid line is the Rietveld fit. The peak position of contributing phase is indicated at the bottom.

Sample 8

A.8 Diffraction patterns of sandstone (sample 8). Scale is Q (2π/d). (A) Stack of 36 diffraction spectra in 2D map plots, comparing experimental data (bottom) with calculated spectra (top) for an image taken at 0∘ tilt and averaged over 10∘ azimuthal intervals. (B) Average diffraction spectrum. Blue dots are measurements and black solid line is the Rietveld fit. The peak position of contributing phase is indicated at the bottom.
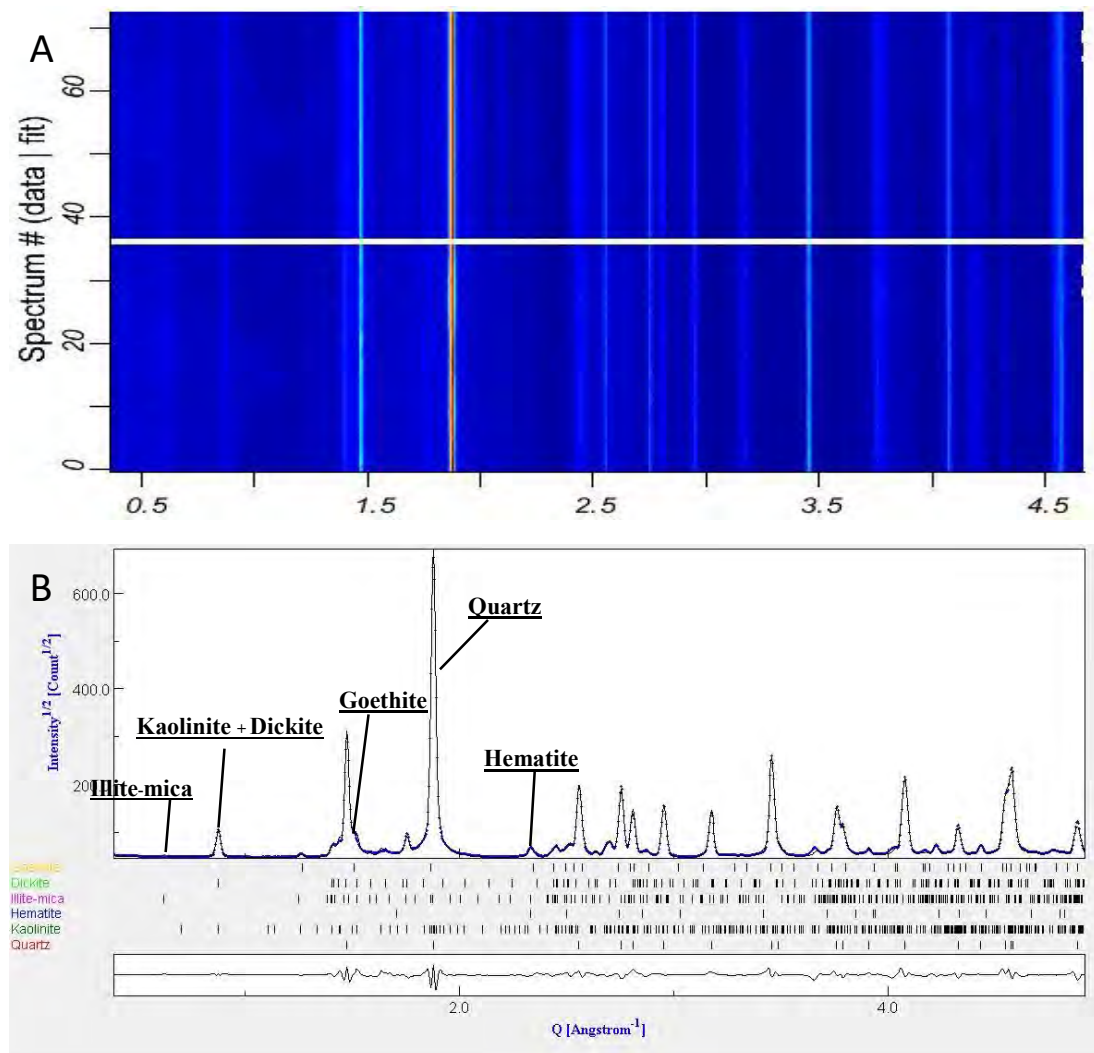
Sample 9

A.9 Diffraction patterns of sandstone (sample 9). Scale is Q ($2\pi/d$). (A) Stack of 36 diffraction spectra in 2D map plots, comparing experimental data (bottom) with calculated spectra (top) for an image taken at $0_\circ$ tilt and averaged over $10_\circ$ azimuthal intervals. (B) Average diffraction spectrum. Blue dots are measurements and black solid line is the Rietveld fit. The peak position of contributing phase is indicated at the bottom.

Sample 10

A.10 Diffraction patterns of Sandstone (sample 10). Scale is Q (2π/d). (A) Stack of 36 diffraction spectra in 2D map plots, comparing experimental data (bottom) with calculated spectra (top) for an image taken at 0∘ tilt and averaged over 10∘ azimuthal intervals. (B) Average diffraction spectrum. Blue dots are measurements and black solid line is the Rietveld fit. The peak position of contributing phase is indicated at the bottom.